High-spin structures in the neutron-rich isotopes $^{57-60}$Mn

D. Steppenbeck,[1,*] A. N. Deacon,[1] S. J. Freeman,[1] R. V. F. Janssens,[2] S. Zhu,[2] M. P. Carpenter,[2] P. Chowdhury,[3] M. Honma,[4] T. Lauritsen,[2] C. J. Lister,[2] D. Seweryniak,[2] J. F. Smith,[1,†] S. L. Tabor,[5] and B. J. Varley[1]

[1]*Schuster Laboratory, University of Manchester, Manchester M13 9PL, United Kingdom*

[2]*Argonne National Laboratory, Argonne, Illinois 60439, USA*

[3]*University of Massachusetts Lowell, Lowell, Massachusetts 01854, USA*

[4]*Center for Mathematical Sciences, University of Aizu, Tsuruga, Ikki-machi, Aizu-Wakamatsu, Fukushima 965-8580, Japan*

[5]*Department of Physics, Florida State University, Tallahassee, Florida 32306, USA*

(Received 31 July 2009; published 14 January 2010; publisher error corrected 6 December 2010)

Excited states in the neutron-rich isotopes $^{57-60}$Mn have been studied with fusion-evaporation reactions induced by ^{48}Ca beams at 130 MeV on ^{13,14}C targets. Level schemes have been deduced reaching spins of $\sim 16\hbar$ and $\sim 27\hbar/2$ in the odd-odd and odd-even isotopes, respectively. States with natural parity within an fp model space are compared to the predictions of large-scale shell-model calculations using the recently developed GXPF1A effective interaction. Quasirotational structures are evident in all of the isotopes and are discussed in terms of the deformation-driving potential of the $\nu 1g_{9/2}$ intruder orbital. It is apparent that an enlarged model space, incorporating at least the $1g_{9/2}$ intruder state, is necessary to reproduce the observed experimental systematics in a more satisfactory manner.

DOI: 10.1103/PhysRevC.81.014305 PACS number(s): 23.20.−g, 21.60.Cs, 27.40.+z, 27.50.+e

I. INTRODUCTION

In recent years, fp-shell nuclei on the neutron-rich side of stability have been studied with great interest on both the experimental and theoretical fronts. The primary motivation for such studies originated from predictions that changes to the well-known shell-model structures of nuclei in and around the valley of stability may occur in exotic nuclear systems. One such example is the discovery of a $N = 32$ subshell closure in ^{52}Ca [1,2], where it was shown that the energy of the 2_1^+ state increases markedly relative to that of the $N = 30$ isotope. Similar structural properties were later observed in ^{54}Ti [3] and ^{56}Cr [4] as well. The energy systematics are accompanied by a strong anticorrelation in $B(E2; 0^+_{\text{g.s.}} \rightarrow 2_1^+)$ transition rates along the isotopic chains of $_{22}$Ti [5] and $_{24}$Cr [6]. Since these observations mirror the situation for the well-known $N = 28$ shell gap, it was concluded that a similar closure also exists at $N = 32$.

One possible explanation for the appearance of new shell closures in exotic nuclei is the proton-neutron (π-ν) monopole interaction [7], which may cause significant modifications to the effective single-particle energies (ESPEs) of orbitals relative to those in the stable and near-stable nuclear systems. The development of the $N = 32$ shell gap may be attributed to the attractive interaction between $1f_{7/2}$ protons and $1f_{5/2}$ neutrons: as protons are removed from the $1f_{7/2}$ orbit, which fills between $Z = 20$ and 28, the magnitude of the interaction decreases, causing the energy of the $\nu 1f_{5/2}$ orbital to shift up relative to the $\nu 2p_{1/2}$ and $\nu 2p_{3/2}$ states. The $N = 32$ shell closure then results as a consequence of a significant $\nu 2p_{3/2}$–$\nu 2p_{1/2}$ spin-orbit splitting in combination with the low level density of the fp shell. In the neutron-rich fp-shell systems with $Z \leqslant 24$ (Ca, Ti, and Cr), the magnitude of the changes in the ESPEs become large enough to the extent that a $N = 32$ subshell closure becomes significant. In the $_{26}$Fe isotopes, however, the $N = 32$ subshell closure is not observed due to the strength of the π-ν interaction.

The energy systematics of the $N = 32$ shell gap is reproduced successfully along isotopic chains of Ca, Cr, and Ti by the GXPF1 effective interaction [8] through a weakening in the strength of the calculated proton-neutron monopole interaction discussed above. The GXPF1 Hamiltonian also predicts a $N = 34$ subshell gap in ^{54}Ca and ^{56}Ti; however, this closure was not observed in recent experimental studies of the neutron-rich Ti isotopes [5,9]. Such a discrepancy between experiment and theory led to the development of a modified interaction, labeled GXPF1A [10], in which adjustments were made to five $T = 1$ matrix elements, mainly involving the $2p_{1/2}$ and $1f_{5/2}$ orbitals. This revised Hamiltonian has been shown to predict the energies of states in the $_{22}$Ti isotopes in a satisfactory manner, including the $J > 6$ states in ^{54}Ti that result from neutron excitations across the $N = 32$ subshell closure.

Recent studies of neutron-rich isotopes in the fp shell include the deduction of yrast and near-yrast structures in $^{54-56}$Ti [3,9,11], $^{55-60}$Cr [12–14], and ^{59,60}Fe [15]. In the interpretations of many of these isotopes, the shape-polarizing effect of the $\nu 1g_{9/2}$ orbital was considered to explain the observations of regular, quasirotational structures at high spin. It is, thus, evident from these studies that population of the $\nu 1g_{9/2}$ intruder orbit has important structural consequences following neutron excitations across the $N = 40$ shell gap.

Gaining new experimental data to compare to the predictions of shell-model interactions like the GXPF1A Hamiltonian is important to help gain a better understanding of the underlying mechanisms involved in the evolution of nuclear

*steppenbeck@riken.jp; Present address: RIKEN Nishina Center, 2-1, Hirosawa, Wako, Saitama 351-0198, Japan.

†Present address: Nuclear Physics Group, University of the West of Scotland, Paisley PA1 2BE, UK.

shell structure away from the valley of stability. High-spin states in neutron-rich fp-shell nuclei have been previously studied using both heavy-ion-induced deep-inelastic and fusion-evaporation reactions, performed under inverse kinematics. In the current work, extensive level schemes are presented for the $^{57-60}$Mn isotopes populated through fusion-evaporation reactions. The decay schemes are compared to shell-model predictions from the GXPF1A effective interaction, and the influence of the $\nu 1g_{9/2}$ orbital on collective aspects at high spin is also discussed.

The lowest-lying yrast states in $^{59-63}$Mn were recently studied through multinucleon transfer reactions, where prompt γ rays were unambiguously associated with particular isotopes using coincidence measurements with ions detected in a high-acceptance magnetic spectrometer [16]. The results presented here are consistent with those given in Ref. [16] for ^{59}Mn but significantly extend that work. The current study also confirms the assignments of γ rays to ^{60}Mn proposed in Ref. [16], but higher $\gamma\gamma$ statistics allow them to be placed in a level scheme. A number of new transitions have also been added, and older work on ^{57,58}Mn [17] has been extended.

II. EXPERIMENTS

Data from two separate heavy-ion fusion-evaporation reactions performed at Argonne National Laboratory were used to study the four neutron-rich Mn isotopes presented in the current work. The experiments are briefly discussed below, though more detailed accounts can be found in Refs. [13–15,18], where the same data sets were used to investigate $^{56-60}$Cr and ^{59,60}Fe.

The Argonne Tandem Linear Accelerator System (ATLAS) was used to generate beams of $^{48}Ca^{11+}$ ions at $E_{\rm lab} = 130$ MeV that were incident on isotopically enriched ^{13}C and ^{14}C targets in the first and second experiment, respectively (hereafter referred to as Expt. I and Expt. II). The resulting compound nuclei were ^{61}Fe and ^{62}Fe, respectively; Mn isotopes resulted from pxn evaporation channels in both experiments.

Prompt electromagnetic radiation from the target position was collected using the Gammasphere array [19], which consisted of 91 and 100 Compton-suppressed HPGe detectors during Expts. I and II, respectively. Reaction residues were separated from the primary beam and dispersed according to their mass-to-charge (A/q) ratio using the Fragment Mass Analyzer (FMA) [20]. The device was optimized to transport $A/q = 59/17$ in Expt. I and $A/q = 60/17$ in Expt. II, but $A/q = 57/16$ also fell into the acceptance in the latter experiment, which is important to the present work for the study of ^{57}Mn. At the focal plane of the FMA, a parallel-plate gridded avalanche counter (PGAC) was used to measure the horizontal and vertical positions of the residues and to generate timing signals. Data acquisition was triggered by the detection of one or more γ rays in coincidence with the arrival of a recoil at the PGAC. Residue energy-loss characteristics were obtained using a segmented-anode ionization chamber located downstream from the FMA. These measurements were used to construct two-dimensional histograms representing the combined energy losses in the first and second anode segments, ΔE, as a function of the total energy loss of an ion, E, within the gas-filled chamber. A two-dimensional $E\Delta E$ spectrum from Expt. II can be found in Fig. 1(b) of Ref. [14], where it can be seen that the Mn group is well resolved from other reaction products of different Z. The γ rays in coincidence with the Mn ions were selected by applying polygonal software gates around the $Z = 25$ group during offline data sorting. The Mn and Fe groups in Expt. I were not fully resolved and, consequently, larger levels of contamination from the xn evaporation channels were unavoidable. In addition to the recoil-γ data, Gammasphere was used in stand-alone mode, i.e., without particle identification, to collect $\gamma\gamma\gamma$ coincidences during both experiments. This allowed the transitions from recoils not accepted through the FMA to be measured, which was important for deducing the structure of ^{58}Mn.

Charge-state ambiguities in A/q spectra were resolved using additional gating techniques that allow selection of particular mass groups by utilizing an ET^2 parameter, where T represents the recoil time-of-flight through the FMA and E is the energy loss discussed above. The methods involved with this technique are already well documented [13–15,18] and will not be discussed in detail here. Two-dimensional histograms of ET^2 versus A/q for the two experiments are shown in Fig. 1 of Ref. [18] and Fig. 1(a) of Ref. [14].

By applying $E\Delta E$ and ET^2 gates simultaneously, it is possible to isolate the γ rays from a given nucleus with only a small level of contamination from other nucleon-evaporation channels. Relevant software gates for the Mn isotopes were applied in this way, and the recoil-$\gamma\gamma$ data were sorted into E_γ–E_γ coincident matrices for analysis. The spectra obtained by applying different gating conditions are shown in Figs. 1(a)–1(d), indicating the quality of selection in Expt. II as an example.

Data from Expt. I were used to construct a level scheme for ^{59}Mn, while those from Expt. II provided the study of ^{57,60}Mn. The triples coincidence data collected from the two experiments were sorted into E_γ–E_γ–E_γ cubes. Since the $A = 58$ mass group was not accepted through the FMA in either experiment, triples coincidences from both data sets were used to build the level scheme for ^{58}Mn. It was found that more ^{58}Mn transitions could be identified in the data set from Expt. I due to the larger relative yield of the $A = 58$ isotope in that experiment.

Transition multipolarities were deduced using both angular-distribution and DCO-ratio (directional correlation of oriented nuclei) analyses. Experimental angular distributions, $W(\theta)$, were fitted to the equation:

$$W(\theta) = A_0 \left[1 + a_2 P_2(\cos\theta) + a_4 P_4(\cos\theta)\right], \qquad (1)$$

where $P_{2,4}(\cos\theta)$ are Legendre polynomials. The $a_{2,4}$ coefficients were used to determine γ-ray multipolarities. Whenever a statistically significant a_4 coefficient could not be extracted, fits of the form $W(\theta) = A_0 \left[1 + a_2 P_2(\cos\theta)\right]$ were adopted. For transitions with relatively low intensities, Gammasphere ring spectra with similar values of $\cos^2\theta$ (for example, Rings 7 and 11, 8 and 10, and 9, with $\cos^2\theta = 0.035$, 0.026, and 0.000, respectively) were summed together to produce three-point angular distributions whenever possible. The sign of the a_2

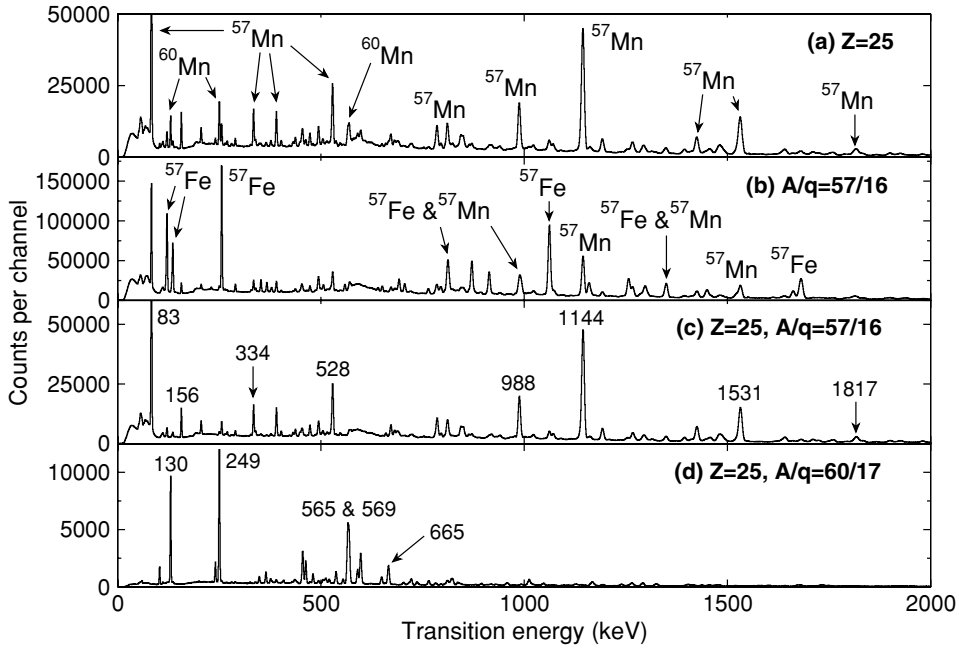

FIG. 1. Spectra illustrating the reduction in the level of background and contamination through the use of different Z and A/q gates. These particular examples used data from Expt. II. The spectra are labeled by the gating conditions used. In spectra (c) and (d), the peaks are assigned to ^{57}Mn and ^{60}Mn, respectively. The energies of the γ-ray lines are given to the nearest keV. Only the most intense transitions have been labeled in order to avoid clutter in the diagram.

coefficient for various weak transitions could be extracted in this way.

DCO ratios, $R_{\rm DCO}$, are defined by the formula:

$$R_{\rm DCO} = \frac{I^{\gamma_2}_{\theta_1}[\mathrm{Gate}^{\gamma_1}_{\theta_2}]}{I^{\gamma_2}_{\theta_2}[\mathrm{Gate}^{\gamma_1}_{\theta_1}]}, \qquad (2)$$

where, for example, $I^{\gamma_2}_{\theta_2}[\mathrm{Gate}^{\gamma_1}_{\theta_1}]$ represents the measured intensity of transition γ_2 in detectors at angle θ_2 with the condition of setting coincidence gates around transition γ_1 in detectors at θ_1. The transition intensities were measured from matrices in which γ rays detected at angles around 90° relative to the beam line (detectors at $\theta = 79.1°$, 80.8°, 90.0°, 99.3°, and 100.8°) were incremented against those detected at angles close to the beam line (detectors at $\theta = 31.7°$, 37.3°, 142.6°, 148.3°, and 162.7°).

The primary criteria used for assigning spins in the level schemes were the measured a_2 and a_4 coefficients, supported by the measured DCO ratios where available. These two pieces of experimental information are generally consistent within the errors involved. Most transitions were identified by this method as stretched $\Delta J = 2$ or $\Delta J = 1$ γ rays with small mixing ratios. A small number of transitions of other types were found and are discussed in detail in the relevant sections. The existence of several parallel-decay pathways between many of the states populated proved useful in restricting the level spins in some cases. Some tentative spin assignments are suggested on the basis of γ-ray intensities and yrast-feeding arguments. Polarization measurements of γ rays were not made here, so any parity assignments rely on those of previous works and/or model-dependent arguments. For example, stretched $\Delta J = 2$ transitions are assumed to be $E2$ in nature. In some other cases, comparisons of experimental levels with the results of shell-model calculations suggest tentative assignments of spin and parity; these are presented in the discussions of the calculations.

III. RESULTS

This work extends previous level schemes for all four isotopes. In the cases of ^{59,60}Mn, no information on yrast states was available prior to the completion of the present study. In fact, only three excited states were identified in each of these isotopes [21–23]. More recently [16], some of the Mn isotopes relevant to the work presented here were populated in a ^{70}Zn + ^{238}U multinucleon transfer reaction at Legnaro National Laboratory (LNL). Although the number of $\gamma\gamma$ coincident events in that experiment was somewhat limited, the proposed transition energies for ^{59,60}Mn, as well as the level scheme for ^{59}Mn, are in good agreement with the results presented here. In general, the level schemes deduced in the current work display many parallel-decay pathways. The transition orderings and level energies are thus given with confidence, as there are ample opportunities for energy- and intensity-sum consistency checks within the level schemes.

A. Odd-even isotopes

1. ^{57}Mn *level scheme*

The level scheme for the $A = 57$ isotope, which was deduced using $Z = 25$, $A/q = 57/16$ recoil-gated $\gamma\gamma$ coincidence data from Expt. II, is presented in Fig. 2. Three distinct sections of the level scheme are labeled A–C. Details regarding the energy levels and transitions are listed in Table I, and examples of γ-ray angular distributions are displayed in Figs. 3(a)–3(d). Figures 4(a)–4(d) summarize some of the evidence for the proposed level scheme, showing spectra obtained from various summed energy gates. Figure 4(a) is gated by transitions in the lower part of Sequence B. The main transitions appearing in the spectrum are from the lower portion of Sequence B and the main band of Sequence A, reflecting the main γ-ray feeding path evident in Fig. 2. Figure 4(b) is gated on transitions in Sequence A and indicates

TABLE I. Energy levels and transitions in ^{57}Mn. All energies are given in keV, and γ-ray intensities (I_γ) are normalized to 100. The a_2 and a_4 coefficients were extracted from angular-distribution measurements. The DCO ratios quoted here were obtained by setting gate limits around the 83-keV transition, with the exception of the value marked with a dagger symbol, which was derived by placing a gate on the 156-keV γ ray. ΔJ represents the assigned spin change in the γ-ray transitions based on the measured $a_{2,4}$ coefficients and DCO ratios. Values marked with an asterisk represent results from unresolved doublets; note that the intensity of the 472-keV line is an upper limit only, since a second transition with the same energy could not be placed in the level scheme.

E_{level} (keV)	J^π	E_γ (keV)	I_γ	a_2	a_4	DCO	ΔJ
82.6(1)	$7/2^-$	82.6(1)	100(3)	−0.35(1)			1
849.6(1)	$3/2^-$	849.6(1)	5.4(1)				
1054.7(2)	$(1/2^-)$	205.0(1)	2.5(1)				
1070.5(2)	$9/2^-$	987.8(1)	19.2(7)	0.27(2)		1.5(2)	(1)
		1069.9(4)	2.0(2)	>0		1.7(8)†	(2)
1226.8(2)	$11/2^-$	156.1(2)	4.6(3)	−0.09(2)			1
		1144.3(1)	69(3)	0.32(1)	−0.08(1)	1.3(1)	2
1374.5(3)	$(5/2^-)$	524.9(2)	1.6(1)				
1477.9(2)	$9/2^-$	1394.0(5)	2.3(2)	−0.07(4)			1
		1478.1(2)	7.0(12)	0.47(5)	−0.14(6)		2
1914.5(2)	$11/2^-$	436.6(1)	2.3(2)	−0.45(6)			1
		687.2(3)	1.7(1)				
		844.0(1)	6.4(3)				
		1832.5(14)	1.0(2)				
1961.7(6)		907.1(5)	0.29(4)				
2186.0(6)		811.5(4)	0.66(8)				
		1131(3)	0.05(3)				
2419.3(2)	$13/2^-$	504.5(2)	0.97(9)	−0.53(8)*			1
		941.6(3)	1.3(2)				
		1192.6(1)	11.1(4)	0.10(2)		1.2(3)	(1)
		1348.5(2)	4.0(2)	0.31(3)			2
2522.6(5)	$(11/2^-)$	1295.6(4)	2.8(2)	0.37(3)*	−0.08(3)*		(0)
		1453.8(10)	0.95(17)				
2711.8(2)	$13/2^-$	1485.1(2)	7.1(3)	0.42(5)			(1)
		1640.8(2)	6.1(3)	0.35(4)	−0.13(5)		2
2757.7(2)	$15/2^-$	337.8(3)	0.50(6)				
		1531.1(1)	47.8(15)	0.42(1)	−0.15(1)	1.5(2)	2
2936.9(3)	$13/2^{(-)}$	1022.6(9)	0.52(10)				
		1709.5(4)	3.8(2)				
3206.0(2)	$15/2^-$	269.0(2)	0.49(5)	−0.16(10)			1
		448.1(3)	0.71(8)	>0			(0)
		494.3(2)	1.8(1)	−0.14(3)			1
		786.9(3)	0.65(17)				
		1292.0(4)	2.0(2)	0.37(3)*	−0.08(3)*		2
		1979.3(6)	1.9(2)	>0			(2)
3253.4(5)	(11/2)	2026.9(16)	0.27(4)				
		2182.2(6)	0.05(4)				
3457.4(3)	13/2	203.8(4)	0.19(5)				
		933.8(23)	0.18(4)				
		2230.6(3)	7.2(3)	−0.17(3)		0.9(4)	1
3677.1(2)	$15/2^{(-)}$	919.4(1)	2.6(2)				
3847.5(2)	15/2	389.9(2)	6.9(2)	−0.09(2)		1.2(3)	1
		1090.4(5)	0.64(8)	>0			(0)
		1135.5(2)	3.0(1)				
3993.1(6)	(13/2)	2767.4(16)	0.86(16)	<0			(1)
4179.3(6)	$17/2^-$	1760.1(4)	3.6(2)	0.32(5)	−0.10(7)		2
4181.8(2)	17/2	333.6(3)	7.1(2)	−0.14(2)		1.2(3)	1
		504.7(1)	2.0(2)	−0.53(8)*			1
		724.4(23)	0.14(6)				
		975.9(3)	0.30(8)				
		1424.2(1)	19.6(6)	−0.13(2)		1.2(3)	1
4200.6(17)	(13/2)	2973.0(15)	0.61(15)	<0			(1)

TABLE I. *(Continued.)*

E_{level} (keV)	J^π	E_γ (keV)	I_γ	a_2	a_4	DCO	ΔJ
4203.5(6)		1444.8(8)	0.41(13)				
4394.7(6)	(15/2)	401.6(2)	0.54(7)				
		1636.7(5)	0.93(12)				
		1683.2(9)	0.46(7)				
4480.5(4)	$(17/2^-)$	1273.4(5)	1.1(1)				
		1723.2(3)	0.39(12)				
4574.8(3)	$19/2^-$	1817.1(1)	10.0(4)	0.41(3)	−0.14(4)	1.4(5)	2
4624.1(15)	$(17/2^-)$	1866.3(12)	0.66(12)				
		1913(3)	0.32(14)				
4631.3(17)	(15/2)	430.7(2)	0.67(7)				
		1920(3)	0.24(8)				
4657.1(5)		453.5(3)	0.43(5)				
		1899.7(4)	1.9(2)	>0			
4710.2(2)	19/2	528.4(1)	20.1(6)	−0.10(1)		0.9(2)	1
		862.6(10)	0.28(7)				
4867.0(6)	(17/2)	472.3(1)	2.0(1)*				
		874(3)	0.24(13)				
		2110.5(16)	0.5(3)				
5177.9(17)	(17/2)	546.6(3)	0.56(6)				
		2426(4)	0.21(13)				
5208.4(14)	$(19/2^-)$	2450.7(11)	1.1(1)				
5338.7(5)		681.6(2)	1.5(1)				
5495.7(2)	21/2	785.5(1)	11.7(4)	−0.05(2)		1.1(3)	1
		1315.1(7)	0.85(10)	0.36(7)	−0.17(8)		2
5526.3(7)	(19/2)	659.3(2)	0.99(7)				
		1132(3)	0.18(8)				
5685(7)		1838(5)	0.11(9)				
5897.3(18)	(19/2)	719.4(4)	0.72(6)	<0			(1)
5962.5(5)		623.3(10)	0.13(4)				
		1252.3(4)	1.2(1)				
6167.3(2)	23/2	671.5(1)	5.5(2)				
		1457.4(2)	2.8(1)	0.39(4)	−0.17(5)		2
6278.6(9)	(21/2)	752.2(6)	0.26(4)				
		1411(3)	0.18(3)				
6629.4(25)	(21/2)	732.1(13)	0.12(3)				
6716.1(11)	$(23/2^-)$	2141.4(8)	1.6(1)	>0			(2)
6799.1(15)		2088.9(11)	0.50(8)				
6969.0(9)	(23/2)	690.3(7)	0.20(4)				
		1442.8(5)	0.05(1)				
7154.8(7)	(25/2)	1659.0(5)	0.79(13)				
7194.1(12)	$(23/2^-)$	2619.3(9)	0.44(13)				
8354.0(14)	(27/2)	2186.7(10)	0.74(8)				

that the flux feeds into Sequence B mainly at the 2758-keV level via the 1424-keV transition, although some other links are clearly present. The third panel shows a spectrum gated on the upper part of Sequence B illustrating the extension of this portion to higher spin. The final panel shows gates set on transitions in Sequence C, revealing that there are several links between this and Sequence B, for example, via the 1485-, 1637-, and 1683-keV transitions.

The most extensive ^{57}Mn decay scheme known prior to the current work was proposed by Appelbe *et al.* [17], where six levels were unambiguously placed along with two further tentative ones. The new results confirm the presence of the 10 γ-ray transitions identified in Ref. [17], including the three tentative lines, although the ordering of the 528- and 1424-keV transitions has been reversed in the current work due to the presence of alternate decay pathways involving the level at 4182 keV. These two γ rays had been ordered only according to their relative intensities in Ref. [17].

Many of the spin assignments in Fig. 2 can be deduced from the $a_{2,4}$ angular-distribution coefficients and DCO ratios listed in Table I. A subset of the assignments that deserve special comment are discussed below.

The ground-state spin and parity of ^{57}Mn are taken to be $J^\pi = 5/2^-$ from β-decay [24,25] and ^{55}Mn(t,p) transfer-reaction [26] experiments. The J^π assignments given in Ref. [17] are in agreement with those proposed here, up to

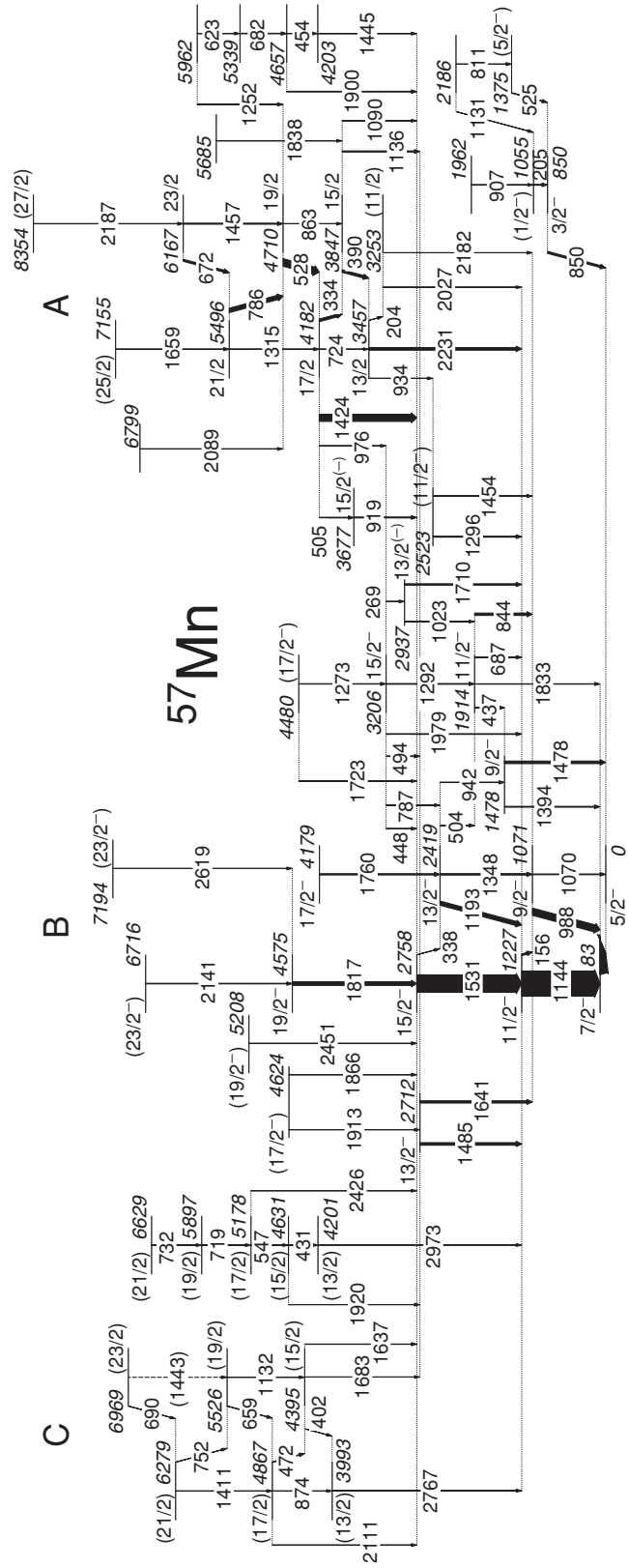

FIG. 2. Level scheme for ^{57}Mn deduced in the present work. Transition and level energies are given to the nearest keV and arrow widths are proportional to transition intensities. States are also labeled by their spin and parity quantum numbers, where known, and tentative assignments are indicated by dashed lines and parentheses.

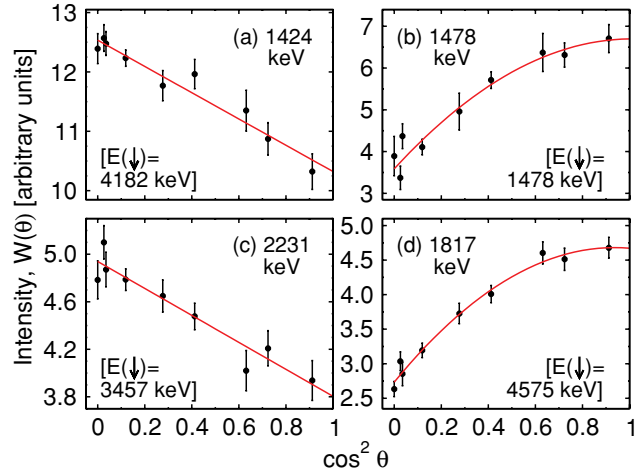

FIG. 3. (Color online) Examples of γ-ray angular distributions in ^{57}Mn. The energies shown at the top of each plot are those of the γ-ray transitions; $E(\downarrow)$ indicates the energy of the state from which each transition depopulates. The solid red lines represent χ^2 minimized fits to experimental data points (filled black circles).

and including the state at 2758 keV. In the current work; however, the 1424-keV γ ray, deexciting the 4182-keV level in Sequence A in the current scheme, is unambiguously assigned as a stretched-dipole transition, as is evident from Fig. 3(a), in contrast to the $E2$ assignment proposed in Ref. [17].

The angular-distribution coefficients of the 83- and 1144-keV transitions, which form a sequence feeding into the ground state, firmly establish the spins of levels at 83 and 1227 keV to be $7/2\hbar$ and $11/2\hbar$, respectively. The 156-keV stretched-dipole transition, deexciting this $11/2\hbar$ state, suggests a $J = 9/2$ assignment for the 1071-keV level, which is partially confirmed by the positive a_2 coefficient associated with the weak 1070-keV γ ray to the $5/2^-$ ground state. Such an assignment then suggests that the 988-keV transition connecting this $9/2\hbar$ state to the $J = 7/2$ level at 83 keV is $\Delta J = 1$. The shape of the angular distribution and the quoted DCO ratio are indeed consistent of such a transition, but with a significant mixing ratio. Similar interpretations can also be made for the 1193- and 1485-keV transitions, since the levels at 2419 and 2712 keV are both fixed to be $J = 13/2$ from alternate decay pathways.

The parities of the states in Sequence B are assigned to be negative. Parities of some of the lower-lying states have been determined in ^{55}Mn(t,p) transfer reactions [26], namely the states at 0, 83, 1071, 1227, 1478, and 1914 keV. These assignments have been extended through the sequence on the basis that the stretched-$\Delta J = 2$ γ rays are likely to be $E2$ transitions. The parity of Structure A cannot be determined using the current experimental data; all transitions linking the main sequence to states of known parity are $\Delta J = 1$ transitions, which could be $M1$ or $E1$. The presence of $\Delta J = 2$ transitions in the bands in Part A does, however, suggest a common parity for the structure.

The spins and parities of the low-lying nonyrast states, shown on the far right of the level scheme, were not deduced

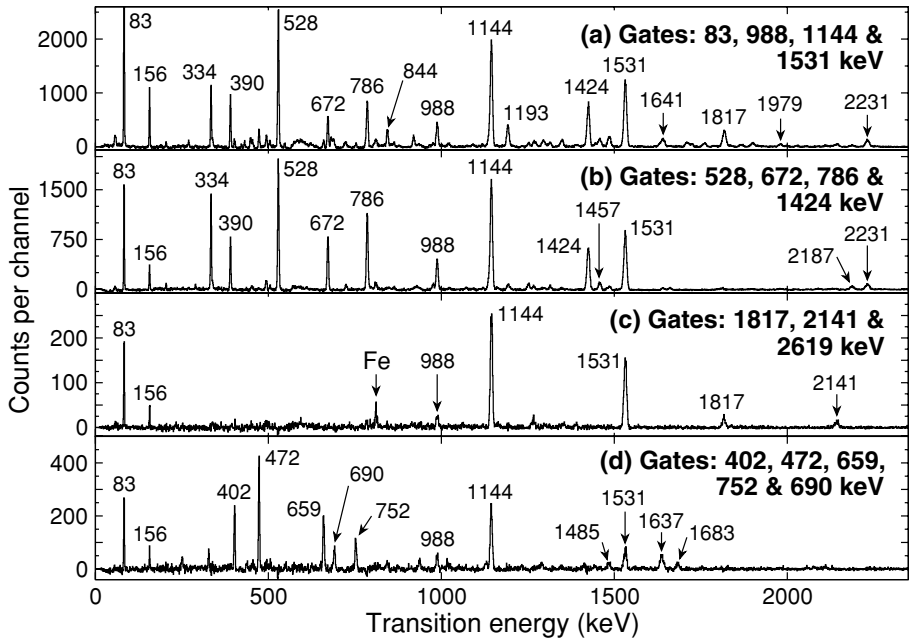

FIG. 4. ^{57}Mn-gated spectra obtained from recoil-$\gamma\gamma$ coincidences. Peaks are labeled by their energy to the nearest keV, and the energy range is the same for all spectra. The individual gated spectra have been summed together to generate the spectra shown here. A contaminant transition is labeled "Fe."

in the current work. Rather, they were taken from β-decay studies of ^{57}Cr [27] together with the results of ^{55}Mn(t,p) [26] and ^{54}Cr(α,p) [28,29] transfer-reaction experiments. Using the results of these studies, the states at 850, 1055, and 1375 keV have been assigned as $3/2^-$, $1/2^-$, and $5/2^-$, respectively, though the latter two J^π values are given only tentatively. Furthermore, the spin and parity of the 2186-keV state are limited to either $1/2^-$, $3/2^-$, or $5/2^-$ given the observed γ-ray branching and the fact that the level is directly populated following the β^- decay of ^{57}Cr.

Where angular-distribution measurements were not possible, some tentative spin assignments are proposed using energy-level systematics, parallel-decay pathways, γ-ray intensities, and yrast-feeding arguments. For example, the states at 6716, 7155, and 8354 keV are given tentative assignments of $J = 23/2$, $25/2$, and $27/2$, respectively, on the assumption that the 2141-, 1659-, and 2187-keV γ rays continue the series of stretched-quadrupole transitions observed in the regular sequences below. Multiple parallel-decay pathways allow tentative spin assignments to be made for states on the left-hand side of Fig. 2 on the basis of limiting spin changes to $2\hbar$ or less.

In a few cases, good correspondence between the measured levels and states from shell-model calculations indicates possible assignments; these are discussed in the following section.

2. ^{57}Mn *shell-model calculations*

The proposed negative-parity states in ^{57}Mn are compared to the predictions of the GXPF1A Hamiltonian in Fig. 5; it can be seen that the level of agreement between the calculations and the experimental results is generally excellent. The root-mean-squared (rms) deviation of the calculated level energies from those deduced experimentally is 119 keV when only states with unambiguous spin and parity assignments are considered, increasing to 139 keV when states with tentative assignments are included as well. Some tentative assignments may be proposed on the basis of good correspondence between experimental and calculated levels. The experimental states at 2523, 2937, and 3677 keV are likely to have spins and parities of $11/2^-$, $13/2^-$, and $15/2^-$, respectively, where the parity assignments are based on good agreement between experimental and calculated states of the same spin. The respective states at 4480, 4624, and 5208 keV are likely to be $17/2^-$, $17/2^-$, and $19/2^-$ due to the good agreement between the measured and calculated energies and γ-ray branching ratios; such assignments are consistent with the expectations of yrast feeding and $\Delta J \leqslant 2$.

With the exception of one minor discrepancy regarding the relative positions of the $13/2^-_2$ and $15/2^-_1$ states, the ordering of all states is reproduced correctly. It should be noted, however, that the difference in energy between the $13/2^-_2$ and $15/2^-_1$ states is only 46 keV experimentally and, thus, such a discrepancy in the shell-model predictions is not surprising given the magnitude of the rms deviation. In addition, the calculations successfully account for the relatively large energy gaps between, for example, the 83/850-, 1478/1914-, 3206/3677-, and 4624/5208-keV pairs of states.

In the high-spin region of the decay scheme, the experimental states become increasingly compressed with respect to their theoretical counterparts. For example, the tentative $23/2^-_1$ and $23/2^-_2$ levels at 6716 and 7194 keV lie 217 and 284 keV below their closest theoretical counterparts, respectively. Such effects may be indicative of an overly restricted model space; however, the effect in ^{57}Mn is not as significant as in more neutron-rich species and the shell-model calculations, at least at lower spins and excitation energies, are generally satisfactory.

There are a number of states in the level scheme, such as those in Parts A and C in Fig. 2, where it is difficult to find any reasonable analogues in the shell-model calculations. Indeed, any attempts to suggest theoretical equivalents from the

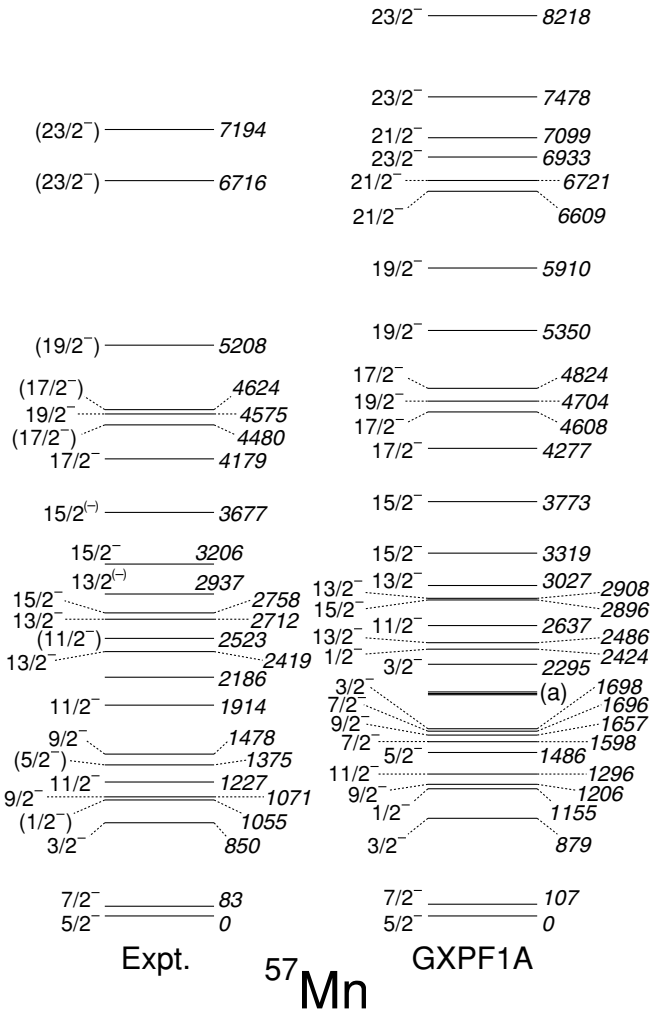

FIG. 5. GXPF1A shell-model calculations for ^{57}Mn compared with experimental results from this work; note that only the negative-parity states are shown here. A maximum of three energy levels are shown for each spin for the sake of clarity. The triplet of states labeled (a) in the GXPF1A column represents one $5/2^-$ state at 2015 keV, one $11/2^-$ state at 2024 keV, and one $9/2^-$ state at 2035 keV.

calculations result in significant increases in the rms deviation noted above. It is, therefore, likely that such excitations involve orbitals beyond the fp model space, such as the $\nu 1g_{9/2}$ intruder state. Further experimental work would be required to confirm such suggestions, but the development of regular sequences may be associated with an increasing polarization of soft nuclear cores by such high-j particles, as has already been observed in Cr and Fe isotopes [13–15].

3. ^{59}Mn *level scheme*

The ^{59}Mn level scheme deduced in the present work is given in Fig. 6, with details regarding the transitions and energy levels listed in Table II. In this case, the structure of the nucleus was derived using $Z = 25$, $A/q = 59/17$ recoil-gated $\gamma\gamma$ coincidence data from Expt. I. Different sequences in the level scheme are labeled A to D; the first three portions show some similarity with sections of the level scheme of ^{57}Mn with a common label.

Figures 7(a)–7(d) give examples of spectra obtained by placing energy gates on the ^{59}Mn transitions, indicating the quality of the data and summarizing how some of the main features of the level scheme were deduced. Spectrum (a) shows gates on some of the transitions in Sequence B. The peaks found in this gate include strong transitions from Sequences A and D, indicating that the main γ-ray flux feeds via both these structures into the low-lying states, in contrast to ^{57}Mn where a structure analogous to A feeds directly into the lower states and there is no analog for Sequence D. Figures 7(b) to 7(d) give gates on transitions at higher spins in Sequences A, C, and D, respectively. The gate on transitions in Sequence A illustrates the strong feeding of lower-lying states by the appearance of peaks corresponding to transitions in B but additionally the presence of transitions linking A to D, for example, the 594-keV line between the 4268-keV state in A and the 3673-keV state in D. This indicates some cross-talk toward the bottom of these structures. Figure 7(b) also displays evidence for the sequence of transitions on the extreme right of Fig. 6, which decay into Sequence A, such as the 1720-keV transition. Figure 7(c) indicates that Sequence C feeds directly into B at the 2922-keV level, as can be seen by the presence of transitions in Sequence C above this point and the corresponding low-lying transitions in B. Spectrum (d) shows a gate on the 181-keV transition in Sequence D, deexciting the state at 3219 keV. This shows evidence for the weaker deexcitation path from the bottom of Sequence D into the lower portion of Sequence B via the two transitions with energies of 1440 and 1692 keV.

In a recent publication [16], yrast states in ^{59}Mn were proposed up to the $J^\pi = 15/2^-$ level at 2920 keV. The level scheme suggested in Ref. [16] was constructed by placing the observed transitions according to energy and intensity systematics as the $\gamma\gamma$ yield was too low to perform coincidence measurements. Despite this, the γ-ray energies, spin-parity assignments and general layout of the decay scheme from the previous study and that proposed here are in agreement. The current data has added significant extensions to the previous scheme.

Angular-distribution analyses were performed, but the lower yields compared to ^{57}Mn restricted the number of instances where this was possible. The low number of $\gamma\gamma$ events also ruled out DCO analyses. The ground-state spin and parity of the $A = 59$ isotope is known to be $5/2^-$ from β-decay studies by Oinonen *et al.* [30]. The level at 112 keV is unambiguously assigned $J = 7/2$ due to the stretched-dipole character of the 112-keV γ ray. The parity of this state is taken to be negative through comparisons with the observed systematics in other odd-A Mn isotopes and shell-model predictions. The spins and parities of the states at 1301 and 2922 keV are unambiguously assigned $11/2^-$ and $15/2^-$, respectively, as a result of the stretched-quadrupole character of the 1189- and 1621-keV transitions. The level at 1049 keV is then assigned $J^\pi = 9/2^-$ due to the stretched-dipole nature of the 253-keV γ ray, which, in turn, fixes the 937-keV γ ray as a $\Delta J = 1$ transition. In much the same fashion as was observed for the analog 988-keV ^{57}Mn line, the positive

TABLE II. Energy levels and transitions in ^{59}Mn. All energies are given in keV, and γ-ray intensities (I_γ) are normalized to 100. The a_2 and a_4 coefficients were extracted from angular-distribution measurements. ΔJ represents the assigned spin change in the γ-ray transitions based on the measured $a_{2,4}$ coefficients and DCO ratios. Values marked with an asterisk represent results from unresolved doublets.

E_{level} (keV)	J^π	E_γ (keV)	I_γ	a_2	a_4	ΔJ
112.1(1)	$7/2^-$	112.1(1)	100(3)	−0.19(2)		1
1048.5(1)	$9/2^-$	936.6(1)	26.2(13)	0.62(7)		(1)
		1048.5(4)	0.6(5)			
1300.9(1)	$11/2^-$	252.5(1)	13.6(5)	−0.31(9)		1
		1188.7(1)	76(3)	0.32(5)	−0.16(6)	2
1861.7(2)	$(9/2^-)$	560.8(1)	5.2(4)			
2343.2(2)	$(11/2^-)$	481.6(1)	2.4(3)			
2640.6(3)	$(13/2^-)$	1340.5(4)	7.6(7)			
		1592.2(4)	1.3(5)			
2722.3(2)	$(13/2^-)$	379.1(1)	1.4(2)			
2740.8(3)	$(11/2)$	1440.0(10)	2.7(8)			
		1691.5(5)	4.3(10)			
2922.0(2)	$15/2^-$	281.9(3)	1.1(2)			
		1621.1(1)	54.7(22)	0.19(5)	−0.09(6)	2
3038.2(3)	$(13/2)$	297.4(1)	5.6(3)	−0.10(4)*		1
3190.3(4)	$(13/2)$	550.0(10)	0.51(18)			
		1890.8(7)	4.9(7)			
3219.4(2)	$(15/2)$	181.2(1)	5.6(3)			
		297.5(1)	23.7(9)	−0.10(4)*		1
		478.7(2)	0.25(21)			
3452.1(4)	$(15/2)$	261.9(1)	2.9(2)	<0		(1)
3673.3(3)	$(17/2)$	454.2(2)	21.3(8)			
3681.7(3)	$(17/2)$	759.7(1)	7.1(5)			
3766.9(5)		1126.3(3)	2.3(5)			
3874.0(3)	$(17/2)$	422.0(2)	2.8(2)	−0.33(14)		1
		951.1(3)	20.1(10)			
4267.7(3)	$(19/2)$	393.6(1)	18.5(7)	−0.26(6)		1
		594.5(3)	5.5(3)			
		1047.4(6)	2.2(3)			
4344.2(3)	$(19/2)$	470.0(2)	1.9(3)			
		671.2(2)	8.3(4)			
4368.0(3)	$(19/2)$	686.3(1)	4.5(4)			
		1445.9(3)	3.0(5)			
4988.3(4)	$(21/2)$	644.5(3)	0.56(21)			
		720.5(2)	9.7(5)			
		1315.3(4)	3.8(4)			
5186.5(4)	$(21/2)$	842.3(6)	1.5(3)			
		918.8(2)	1.0(3)			
5238.2(3)	$(21/2)$	870.3(2)	3.9(4)			
		1556.5(3)	1.9(4)			
5800.8(5)	$(23/2)$	812.5(2)	5.8(4)			
		1456.2(8)	2.2(4)			
5987.8(7)	$(23/2)$	1719.5(9)	3.6(5)			
6234.5(4)	$(23/2)$	996.2(1)	2.6(5)			
		1866.5(3)	1.1(3)			
6681.8(4)		447.3(1)	1.9(2)			
6785.2(7)	$(25/2)$	797.4(2)	1.4(4)			
		1797.5(6)	1.0(4)			
7146.7(5)	$(25/2)$	912.3(2)	2.0(4)			
		1908.5(10)	2.8(6)			
7321.3(23)		1520.5(16)	1.3(4)			
7458(10)		1657(7)	0.3(3)			
7607.7(11)		1806.9(7)	0.9(5)			
7749.9(7)	$(27/2)$	965.4(10)	0.3(3)			
		1948.9(4)	0.8(5)			
7758.2(15)		611.5(10)	4.1(3)			

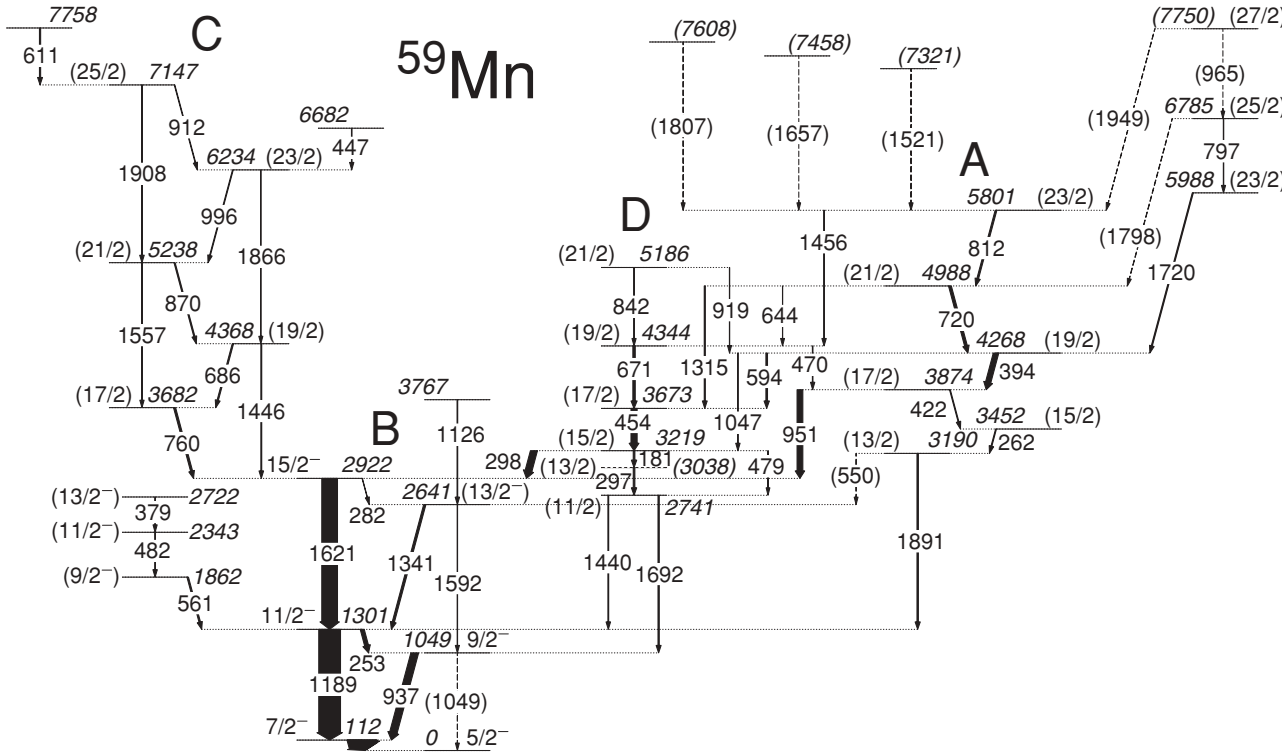

FIG. 6. Level scheme for ^{59}Mn; transition and level energies are given to the nearest keV and arrow widths are proportional to transition intensities. States are also labeled by their spin and parity quantum numbers, where known, and tentative assignments are indicated by dashed lines and parentheses.

a_2 coefficient of the 937-keV γ ray is consistent with a $\Delta J = 1$ transition with a large mixing ratio.

There is an obvious similarity between the level scheme of ^{59}Mn and that previously discussed for ^{57}Mn with the presence of three analogous structures labeled A–C in Figs. 2 and 6. For example, the γ-ray energies and relative intensities are very similar in the low-lying sequences built above the $5/2^-$ ground states (Sequence B). In addition, coupled-band sequences (A and C) appear in both level schemes. In ^{59}Mn, Sequence A consists of a series of transitions with energies 262, 422, and 394 keV, all with negative a_2 coefficients, paralleling the analogous sequence in ^{57}Mn. The nonobservation of the

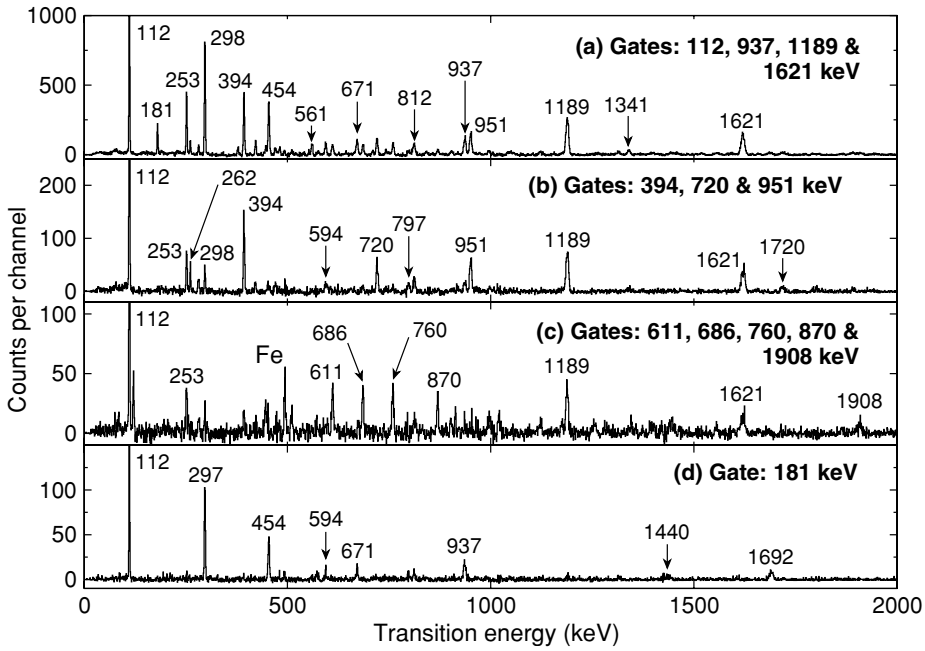

FIG. 7. ^{59}Mn-gated spectra obtained from recoil-$\gamma\gamma$ coincidences. Peaks are labeled by their energy to the nearest keV. The occurrence of more than one gate implies that the individual gated spectra have been summed together. The transition marked with "Fe" is a contaminant from ^{59}Fe.

associated $\Delta J = 2$ γ rays in ^{59}Mn is consistent with the branching ratios from analogous states in ^{57}Mn and the inferior level of statistics available in the $\gamma\gamma$ matrix used to build the ^{59}Mn level scheme. Even though these likely-$E2$ transitions were not observed, it is probable that the states in Sequence A in ^{59}Mn all have the same parity. The sequences labeled A in both nuclei, connected by these transitions, have parallel-decay pathways to the lower-lying negative-parity states, although statistically significant angular distributions for the 951- and 1891-keV transitions deexciting the respective states at 3874 and 3190 keV in ^{59}Mn could not be obtained. The levels at 4988 and 5801 keV in ^{59}Mn are tentatively given as $J^\pi = 21/2$ and $23/2$, based on the assumption that the 720- and 812-keV γ rays continue the series of stretched-dipole transitions observed below.

Lack of statistics and contamination from ^{59}Fe prevented angular-distribution analyses of the other transitions. Some states were tentatively assigned J^π values by considering systematics and yrast-feeding arguments. For example, for the states in Sequence D built above the 2741-keV level, tentative spin assignments were made through considerations of γ-ray relative intensities and yrast-feeding arguments. However, since no independent angular distribution could be measured for the 298-keV transition due to the presence of the unresolved 297-keV γ ray, an assignment of $J = 17/2$ to the 3219-keV level cannot be ruled out. Note also that the ordering of the 181- and 297-keV γ rays is tentative as these two transitions are found to have the same intensities within their experimental uncertainties. If the order of the γ rays were reversed, two separate states must exist at 2922 keV [see Fig. 7(d)], albeit with different spin-parity quantum numbers. The tentative spin assignments for the states in Sequence C are also made on the basis of yrast-feeding arguments. Comparison with shell-model calculations also allows some tentative spin-parity assignments to be made, as detailed in the next section.

It is noted that beyond Sequence B parity assignments are difficult. As noted above, it is likely that the states in Sequence A all have the same parity. The presence of two tentative $\Delta J = 2$ transitions with energies of 1315 and 1047 keV, linking Sequence A to D, suggests a common parity for both structures. It is difficult to determine which parity is most likely from the current experimental measurements; however, comparisons with shell-model calculations gives some speculative insight as discussed below.

4. ^{59}Mn *shell-model calculations and comparisons with* ^{57}Mn

The shell-model predictions for ^{59}Mn are compared to the experimental results in Fig. 8. The agreement between the observed and theoretical systematics are also reproduced rather well for the negative-parity states in this isotope, thus continuing the success of the GXPF1A Hamiltonian to higher mass. In this case, the rms deviation is 86 keV between the states with unambiguous J^π assignments.

A comparison of experimental and shell-model schemes again suggests some tentative spin assignments. For example, the states at 1862, 2343, and 2722 keV agree rather well with predictions of the GXPF1A Hamiltonian and are tentatively assigned $J^\pi = 9/2^-_2$, $11/2^-_2$, and $13/2^-_2$, respectively.

FIG. 8. GXPF1A shell-model calculations for ^{59}Mn compared with experimental results from this work; note that only the negative-parity states are shown here. A maximum of three energy levels are shown for each spin for the sake of clarity.

The rms deviation increases to 110 keV when levels with tentative spin and/or parity assignments are also included. Note that the ordering of the states are reproduced in a satisfactory manner, although the relative positions of the $15/2^-_1$ and $13/2^-_2$ states is reversed in the predictions, as was seen in the case of ^{57}Mn. However, these two calculated levels are separated by only 62 keV and such a discrepancy is, therefore, not surprising. Furthermore, the relatively large energy gaps observed experimentally between the 112/1049- and 1301/1862-keV pairs of states, for example, are also accounted for in a satisfactory way.

There is a possibility that the 3767-keV experimental state at the top of Sequence B corresponds to the predicted $15/2^-_3$ level given the similarity of the empirical and theoretical energies. However, the calculations predict significant γ-ray branching to the $15/2^-_1$ level in addition to the $13/2^-_1$, whereas only the latter is observed experimentally.

As noted above, in the sequence of dipolar transitions built on the ground state in ^{59}Mn with energies of 112, 937, 253, 1341, and 282 keV, the measured angular-distribution coefficient for the $9/2^-_1 \rightarrow 7/2^-_1$ transition is qualitatively consistent with a significant mixing ratio. Shell-model calculations are in agreement with this finding. In the analogous structure in ^{57}Mn, the predicted mixing ratios for transitions deexciting states up to the $15/2^-_1$ level are also in qualitative agreement with experimental angular-distribution coefficients, apart from that of the 1193-keV transition from the $13/2^-_1$ level. In this case, the decay of the $13/2^-_1$ state is predicted to take place via a relatively pure $M1$ transition, whereas the experimental a_2 value suggests a significant $E2$ admixture. It is, therefore, likely that the shell-model calculations slightly underestimate the mixing between the $13/2^-_1$ and $13/2^-_2$ states in ^{57}Mn, since the latter is predicted to have a significant $E2$ component in the transition to the $11/2^-_1$ state.

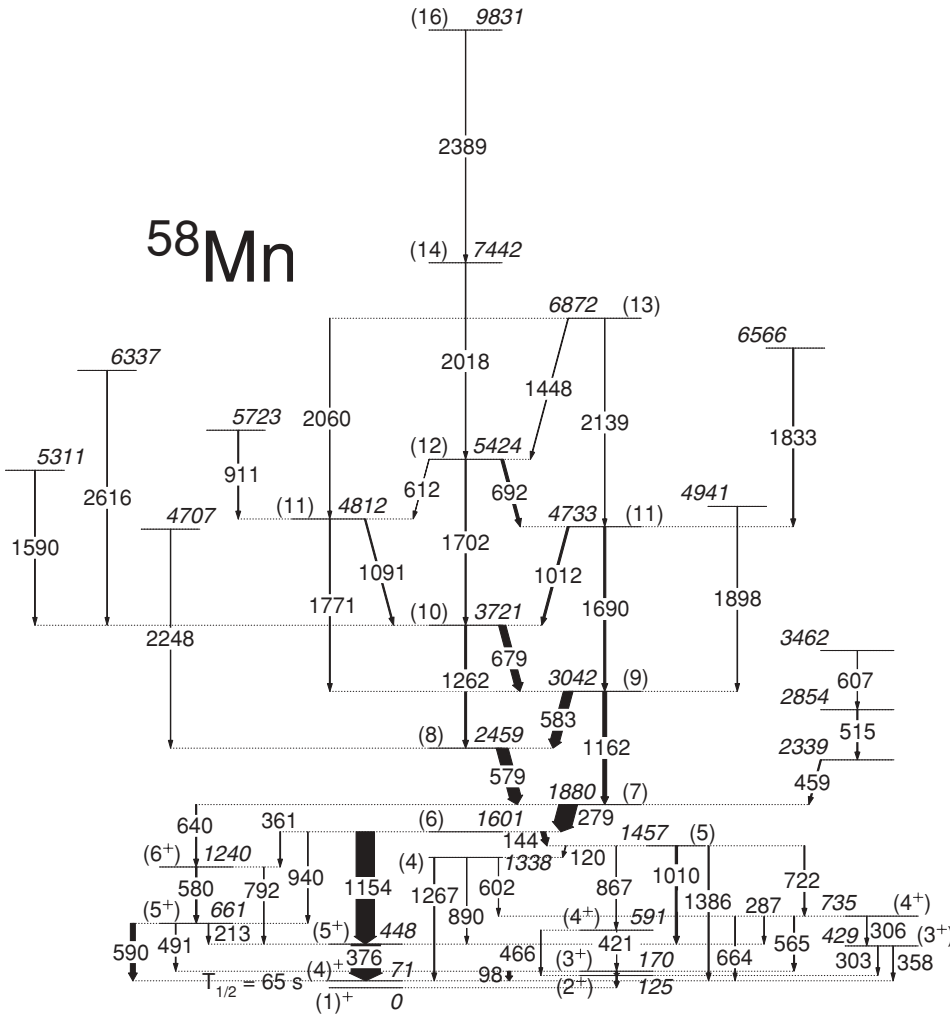

FIG. 9. Level scheme for ^{58}Mn; transition and level energies are given to the nearest keV and arrow widths are proportional to transition intensities. States are also labeled by their spin and parity quantum numbers, where known, and tentative assignments are indicated by dashed lines and parentheses. The unlabeled γ ray that lies between the 170- and 125-keV states is the 44-keV transition.

It becomes difficult to interpret some of the levels around and beyond 3 MeV in ^{59}Mn, particularly those in Sequences A, C, and D, in terms of fp-shell configurations alone, since their excitation energies and γ-ray branchings are inconsistent with those predicted by the GXPF1A interaction. States without clear shell-model counterparts in ^{57,59}Mn are candidates for states resulting from nucleon excitations beyond the fp model space adopted in the GXPF1A predictions. A number of such states appear to form regular sequences: in ^{57}Mn, Sequence C, these are above the tentative $J = 13/2$ states at 3993 and 4201 keV, and above the tentative $11/2$ state at 3253 keV in Sequence A. Similarly, in ^{59}Mn, the states in Sequences A and C have no obvious shell-model counterparts.

It is interesting to speculate whether such regular structures beyond the fp shell involve configurations that include the $\nu 1g_{9/2}$ orbit. Such speculations are particularly tempting as there is some evidence that their excitation energy decreases with increasing neutron number; compare the $13/2$ state at 3457 keV in ^{57}Mn with the state of the same spin in a seemingly analogous sequence in ^{59}Mn, which lies at 3190 keV. Such behavior would be similar to that observed in the Cr and Fe isotopes. A single-neutron excitation to the $1g_{9/2}$ orbit would produce states of positive parity; definitive assignments of the parities of Sequences A–C in both Mn isotopes would allow a firmer conclusion to be reached.

B. Odd-odd isotopes

1. ^{58}Mn *level scheme*

The level scheme for the $A = 58$ isotope, which is proposed in Fig. 9, was deduced using $\gamma\gamma\gamma$ coincidences from Expts. I and II. Specific information regarding the transitions and energy levels are listed in Table III.

Earlier studies of ^{58}Mn revealed the existence of two different metastable states, one with $T_{1/2} = 3$ s and another, longer-lived state with $T_{1/2} = 65$ s [25,31–33], both of which are unstable with respect to β^- decay. It is now accepted that the shorter-lived state is the ground state, while the 65-s isomer is located at $E_x = 71$ keV; the spins and parities of these states are taken to be $(1)^+$ and $(4)^+$, respectively [17,33–35]. The nonobservation of a 71-keV transition between these two levels in the $\gamma\gamma\gamma$ data here is expected given the half-life of the isomeric state.

Figures 10(a)–10(c), where the different spectra were obtained by setting triples coincidence gates, summarize some of the arguments used to build the level scheme. Panel (a) illustrates the main pathway of deexcitation through the level

TABLE III. Energy levels and transitions in ^{58}Mn. All energies are given in keV, and γ-ray intensities (I_γ) are normalized to 100. I_γ values marked with a dagger symbol represent lower limits only. No transition is reported depopulating the 71-keV level here since the state is isomeric.

E_{level} (keV)	J^π	E_γ (keV)	I_γ
71.3(4)	$(4)^+$		
125.5(3)	(2)	125.5(2)	5.0(9)†
169.5(4)	(3)	44.2(3)	4.5(9)
		97.9(3)	10.8(24)
429.2(5)	(3)	303.1(4)	0.49(10)
		358.0(2)	1.1(3)
447.6(4)	(5)	376.1(1)	100(5)
590.8(4)	(4)	421.4(2)	0.64(9)
		465.8(5)	0.08(2)
660.6(5)	(5)	212.8(2)	2.4(3)
		490.9(4)	2.5(3)
		589.8(2)	16.9(23)
734.9(4)	(4)	286.8(2)	0.65(5)
		305.6(2)	0.74(8)
		565.3(2)	3.5(3)
		663.8(2)	0.61(6)
1239.7(5)	(6)	580.0(6)	5.0(5)†
		792.1(3)	1.5(3)†
1337.6(5)	(4)	601.9(5)	0.73(9)
		890.3(2)	0.76(21)
		1266.6(9)	3.5(7)
1457.2(4)	(5)	119.8(4)	2.3(3)
		721.7(2)	3.5(4)
		866.5(2)	0.76(8)
		1009.5(2)	7.6(8)
		1386.2(3)	3.9(4)
1600.9(5)	(6)	143.7(2)	15.9(13)
		361.4(2)	2.7(2)
		940.3(2)	1.8(2)
		1153.5(3)	63(5)
1880.0(5)	(7)	279.0(1)	62(4)
		640.2(2)	3.8(4)
2339.2(5)		459.3(2)	4.2(3)
2459.3(7)	(8)	579.1(5)	40(4)
2854.2(6)		515.0(2)	3.9(3)
3042.2(7)	(9)	582.8(5)	32(4)
		1162.4(5)	13.1(9)
3461.6(7)		607.4(3)	1.0(1)
3720.9(7)	(10)	678.7(1)	24.1(17)
		1261.6(7)	6.6(7)
4707.2(24)		2247.9(17)	1.4(1)
4732.6(7)	(11)	1012.1(4)	7.0(6)
		1690.5(2)	7.1(5)
4811.9(7)	(11)	1090.9(2)	4.5(4)
		1770.6(7)	3.3(2)
4940.6(8)		1898.4(3)	1.9(2)
5311.4(8)		1590.5(3)	1.8(2)
5424.0(7)	(12)	612.0(2)	1.1(1)
		691.6(2)	9.5(7)
		1702.3(4)	4.0(3)
5722.8(8)		910.8(2)	3.4(2)
6336.6(16)		2615.7(11)	0.72(6)
6565.9(10)		1833.3(5)	3.8(3)
6872.1(8)	(13)	1448.2(2)	2.2(2)
		2059.9(12)	0.51(5)
		2138.9(10)	1.5(1)
7442.0(12)	(14)	2018.0(7)	1.8(1)
9830.6(19)	(16)	2388.6(11)	1.3(1)

scheme with gates set on a transition feeding the $(4)^+$ isomer and a transition at the bottom of the coupled structure that dominates the higher-spin regime. The resulting spectrum indicates that the general pattern of feeding is via the relatively strong, regular sequence. The lower-spin region of the level scheme is rather complicated, but the presence of a strong 1154-keV photopeak in this coincidence spectrum indicates the main route to the isomer. There are also many weaker parallel branches through the low-spin region; Fig. 10(b) gives one example that also illustrates the sensitivity to low-energy transitions important in the lower part of the level scheme. Spectrum (c) provides evidence for the presence of the 580-keV triplet; a well-defined γ-ray photopeak can be seen at 580 keV, corresponding to a transition in a weaker parallel route through the lower-spin states (to the left of Fig. 9) when gates are set around the 579- and 583-keV transitions, two of the stronger crossover transitions in the regular band.

In a recent study by Appelbe *et al.* [17], yrast states in ^{58}Mn were populated following a ^{13}C + ^{48}Ca fusion-evaporation reaction. Nine transitions were firmly assigned to the $A = 58$ isotope in that work, the energies of which are in agreement with those proposed here. It should be noted, however, that the current ordering of some of the transitions differs from those published in Ref. [17]. In the new, extended level scheme, many parallel-decay pathways were found that give a high level of confidence to the proposed level energies, whereas some of the transition orderings proposed in Ref. [17] were based solely on γ-ray intensities. For example, the 279-keV γ ray from the state at 1880 keV is placed above the 1154-keV transition. The ordering of the two transitions deexciting the level at 1601 keV, with energies of 144 and 1010 keV, has been reversed relative to that proposed in Ref. [17]. Also, the 1267-keV transition, which was placed running parallel to the 583- and 679-keV γ rays in Ref. [17], is found to feed the isomeric state at 71 keV in the new level scheme. A weaker 1262-keV transition is proposed to run parallel to the two lower-energy γ rays in this work, which agrees better with the energy systematics.

Neither angular distributions nor DCO ratios could be measured for the ^{58}Mn transitions in the current study due to the vast number of stronger contaminant photopeaks, mainly from Fe residues resulting from xn evaporation channels. However, the characteristics of some of the transitions were taken from Ref. [17]. Appelbe *et al.* [17] identified each of the 279-, 376-, 580-, 679-, 1010-, and 1154-keV γ rays as stretched-dipole transitions. Thus, a sequence of stretched-dipole transitions is present above the $J = 4$ isomeric state, which implies that the spins of the associated levels from

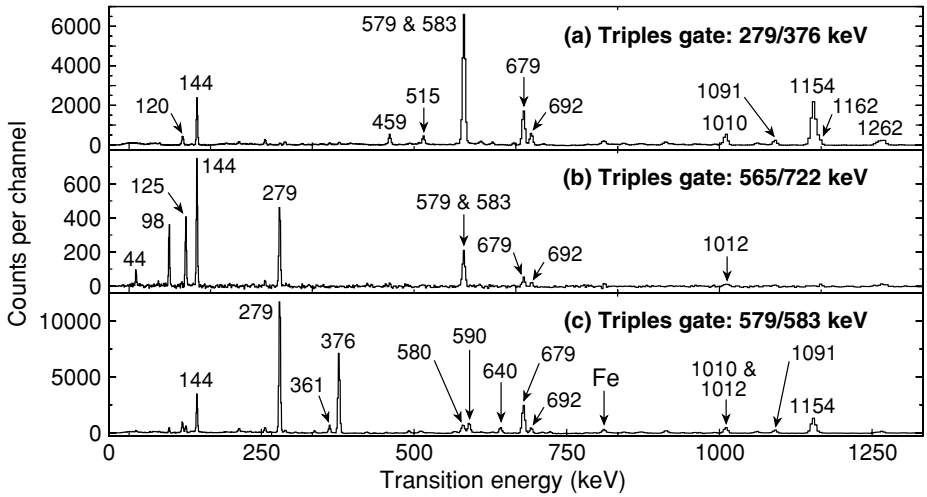

FIG. 10. ^{58}Mn-gated spectra obtained from $\gamma\gamma\gamma$ coincidences. Peaks are labeled by their energy to the nearest keV. A contaminant peak is indicated by "Fe."

448 to 3721 keV are $5\hbar$ to $10\hbar$, respectively. The parities of these states are discussed later. The states at 4733, 5424, 6872, 7442, and 9831 keV are tentatively assigned spins of 11, 12, 13, 14, and $16\hbar$, respectively, on the assumption that there is a continuation in the observed sequence of transitions. Furthermore, the spin of the state at 4812 keV is restricted to $J = 11$, given the observed feeding and depopulating γ rays. The 144- and 120-keV transitions at the bottom of the two bands are also assumed to be part of the sequence above, and the spins of the states at 1457 and 1338 keV are thus proposed to be $5\hbar$ and $4\hbar$, respectively.

2. ^{58}Mn *shell-model calculations*

Although no experimental evidence exists for the assignment of parities to the majority of the states in ^{58}Mn, some experimental levels show good correspondence to the states calculated in a fp model space. These proposed positive-parity states in ^{58}Mn are plotted against the predictions of the GXPF1A effective interaction in Fig. 11.

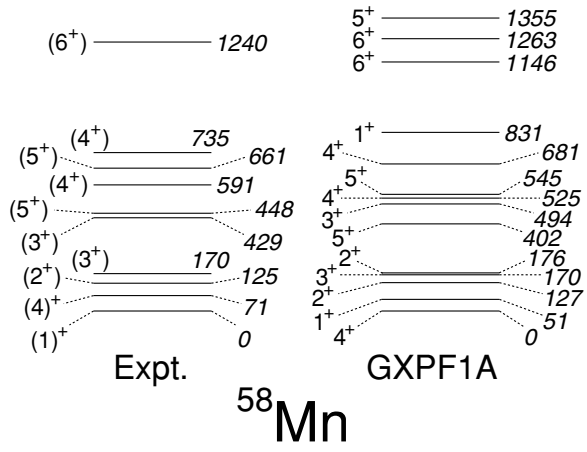

FIG. 11. GXPF1A shell-model calculations for ^{58}Mn compared with the suspected positive-parity experimental results from the current work. A maximum of three energy levels are shown for each spin for the sake of clarity.

Although the GXPF1A calculations predict a 4^+ ground state, the theoretical 1^+ state lies only 51 keV higher in energy, so the contrast to the observed ordering, a ground state with 1^+ followed by a 4^+_1 state at 71 keV, is not truly significant.

Since the multipolarities of the weak transitions below the 1601-keV state could not be deduced here, their most probable J^π quantum numbers could only be suggested by comparing the experimental results to shell-model predictions. In particular, good correspondence suggests positive parity for many of the low-lying, low-spin states. Tentative spin-parities assigned in this way are consistent with the expectations of yrast feeding and reasonable comparisons to the observed γ-decay branching ratios with GXPF1A predictions. The resulting tentative assignments can be found in Fig. 9.

It is difficult to interpret the states above, and including, the level at 1338 keV in terms of the GXPF1A calculations. Although there is a possibility that the 1338- and 1457-keV states may correspond to theoretical nonyrast $J = 5$ or 6 states, there are certain discrepancies between the observed and predicted γ-decay branches that would cause such assignments to be tenuous. Furthermore, the only reasonable potential shell-model counterpart for the level at 1601 keV is the $J^\pi = 7^+_1$ state due to the large decay branch to the yrast 5^+ level. However, such an assignment requires the multipolarity of the 1154-keV transition to be stretched quadrupole, clearly at variance with the negative a_2 value measured by Appelbe *et al.* [17]. Experimental levels without fp shell-model counterparts are clearly candidates for configurations involving the $1g_{9/2}$ orbital. The appearance of such levels at low excitation energy suggests configurations involving one $1g_{9/2}$ neutron, indicating that perhaps the regular, coupled sequence at higher spins, shown in Fig. 9, is of negative parity.

3. ^{60}Mn *level scheme*

Prior to the present work, only three excited states were known in ^{60}Mn. One of these levels was identified as a β-unstable isomer at 272 keV with $T_{1/2} = 1.8$ s [22,33,36]. The remaining states were observed at $E_x = 759$ keV and, tentatively, 349 keV following the β^- decay of ^{60}Cr [23]. The energy of the latter state was uncertain due only to the

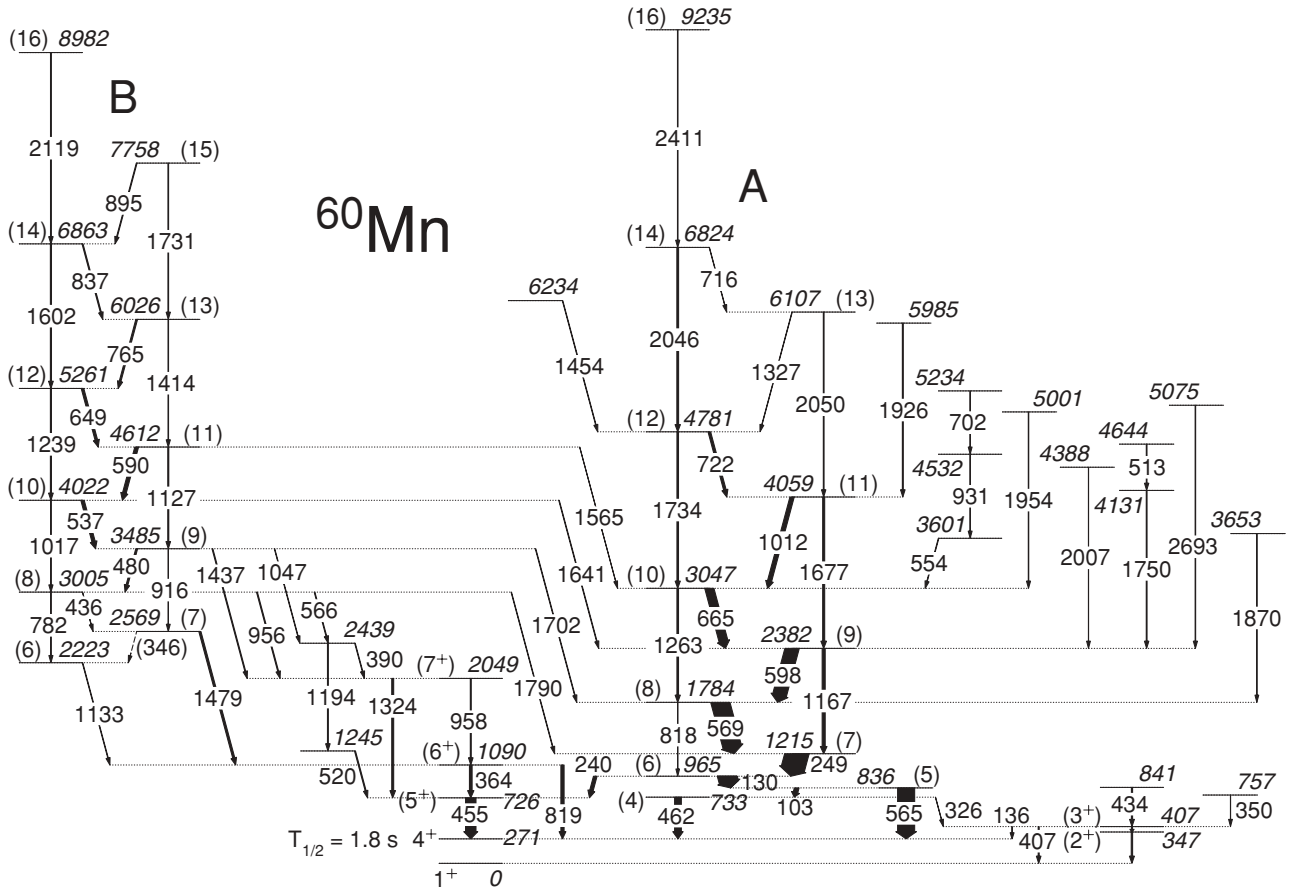

FIG. 12. Level scheme for ^{60}Mn; transition and level energies are given to the nearest keV and arrow widths are proportional to transition intensities. States are also labeled by their spin and parity quantum numbers, where known, and tentative assignments are indicated by dashed lines and parentheses. The unlabeled γ ray that lies between the 407- and 347-keV states is the 60-keV transition.

fact that the intensities of the 349- and 410-keV transitions were measured to be the same to within their experimental uncertainties in Ref. [23]. The spin and parity of the ^{60}Mn ground state were recently deduced by Liddick *et al.* [23] to be 1^+, while those of the 272-keV metastable state are taken to be 4^+ from the studies of Schmidt-Ott *et al.* [34]. More recently, γ-ray transitions from yrast states in the $N = 35$ isotope were observed in the ^{70}Zn + ^{238}U multi-nucleon transfer reaction at LNL [16]. In that work, γ-ray lines were identified at 130, 250, 349, 455, 463, and 568 keV, which are in good agreement with those proposed here. However, these transitions could not be placed in coincidence due to insufficient $\gamma\gamma$ statistics.

The decay scheme for ^{60}Mn proposed here is given in Fig. 12. This is clearly more extensive than previous attempts, and confidence in the proposed level energies is gained through the use of $\gamma\gamma$ coincidence measurements. Specific information regarding the γ-ray transitions and level energies in the $A = 60$ isotope are listed in Table IV. In this case, the level scheme was derived using $Z = 25$, $A/q = 60/17$ recoil-gated $\gamma\gamma$ data from Expt. II. Figures 13(a)–13(d) summarize some of the evidence for the level scheme proposed in the current work. Figures 13(a) and 13(b) provide spectra resulting from gates set on transitions from the bands labeled A and B in Fig. 12, respectively. Spectrum (a) is dominated by transitions within Band A itself, illustrating the main decay path in the nucleus. There are a small number of peaks corresponding to transitions out of the bottom of the band, with energies of 240, 462, and 565 keV, to the lowest observed states. The first of these feeds the state at 726 keV whose decay is also apparent with the presence of a 455-keV transition to the isomeric 4^+ state; the other two transitions feed the 4^+ isomer directly. The decay of the isomer is not observed here; the half-life of 1.8 s, consistent with a spin difference of $3\hbar$ to the ground state, is considerably longer than coincidence times of the data acquisition. The spectrum in Panel (b), gated on Band B, also contains many in-band transitions as expected, but the presence of many other transitions illustrates that it feeds into the lower states at a higher excitation and in a more complicated fashion than Band A. Spectrum (c), which is gated on transitions running parallel to the 565-keV line deexciting the state at 836 keV near the bottom of Band A, shows the 569-keV line in the absence of the 565-keV γ ray. There is a notable reduction in the width of the photopeak and a small shift in the position of the centroid, providing evidence for the presence of two transitions of similar energies. Finally, the spectrum given in Fig. 13(d) is gated on the four higher-energy transitions with energies of 1565, 1641, 1702, and 1790 keV that link Bands

TABLE IV. Energy levels and transitions in ^{60}Mn. All energies are given in keV, and γ-ray intensities (I_γ) are normalized to 100. The a_2 and a_4 coefficients were extracted from angular-distribution measurements. Values marked with an asterisk represent results from unresolved doublets. The DCO ratios quoted here were obtained by setting gate limits around the 249-keV transition. ΔJ represents the assigned spin change in the γ-ray transitions based on the measured $a_{2,4}$ coefficients and DCO ratios. No transition is reported here depopulating the 271-keV level since the state is isomeric.

E_{level} (keV)	J^π	E_γ (keV)	I_γ	a_2	a_4	DCO	ΔJ
271.2(2)	4^+						
347.4(2)	(2^+)	347.6(2)	5.7(4)				
407.2(2)	(3^+)	59.9(2)	2.3(6)				
		135.8(2)	1.3(6)	<0			(1)
		407.0(2)	4.2(14)	>0			(2)
725.8(2)	(5^+)	454.6(1)	44.0(16)	0.15(4)		1.6(5)	(1)
733.3(2)	(4)	325.8(3)	0.96(15)				
		462.1(1)	28.6(11)	0.22(4)		1.3(3)	(0)
756.9(2)		349.7(1)	0.63(22)				
835.9(2)	(5)	102.5(1)	18.7(10)	−0.18(7)		0.9(3)	1
		565.0(2)	72(3)	−0.04(3)*		1.0(1)*	1
841.4(3)		434.2(2)	5.0(5)				
965.4(2)	(6)	129.5(1)	80(3)	−0.18(2)		1.2(2)	1
		239.6(1)	14.7(5)	−0.06(5)		0.9(3)	1
1089.8(3)	(6^+)	364.0(1)	11.2(5)	0.24(8)			(1)
		818.7(9)	13.5(19)				
1214.6(2)	(7)	249.2(1)	100(3)	−0.09(2)			1
1245.3(4)		519.6(3)	4.0(6)				
1783.8(3)	(8)	569.1(2)	79(3)	−0.04(3)*		1.0(1)*	1
		818.4(2)	0.6(5)				
2048.8(3)	(7^+)	958.1(5)	4.0(6)	>0*			
		1323.8(7)	8.1(10)	0.47(12)			2
2222.7(3)	(6)	1132.7(3)	2.1(9)				
2381.6(3)	(9)	597.6(2)	59(2)	−0.06(3)		1.1(2)	1
		1167.2(2)	12.8(7)	0.46(10)	−0.24(12)	1.7(8)	2
2438.5(3)		389.6(3)	2.3(3)				
		1193.5(9)	3.7(4)				
2568.9(3)	(7)	346.2(10)	0.34(11)				
		1479.1(9)	8.8(13)				
3005.0(3)	(8)	436.1(1)	0.93(22)				
		566.5(1)	2.9(4)				
		782.2(2)	2.0(3)				
		956.1(3)	3.8(6)	>0*			
		1790.4(23)	1.9(4)				
3047.0(3)	(10)	665.5(1)	37.8(13)	−0.07(4)		1.0(3)	1
		1263.4(4)	6.7(5)	0.34(9)	−0.23(11)		2
3485.4(3)	(9)	480.4(2)	7.5(6)				
		916.5(15)	1.1(3)				
		1046.9(2)	1.9(3)				
		1436.9(6)	3.6(6)				
		1701.6(3)	2.2(3)				
3601.0(3)		554.0(1)	2.1(3)				
3653.5(5)		1869.6(4)	0.6(5)				
4022.1(3)	(10)	536.6(1)	13.9(8)				
		1016.9(2)	2.3(5)				
		1640.7(3)	2.3(3)				
4058.7(3)	(11)	1011.6(1)	17.7(8)	−0.16(8)		1.4(5)	1
		1676.8(5)	8.4(6)	0.35(13)			2
4131.4(5)		1749.8(4)	3.3(6)				
4388.3(5)		2006.7(4)	0.7(5)				
4532.0(3)		931.0(1)	1.2(3)				
4612.2(3)	(11)	590.0(1)	15.5(8)	<0			(1)
		1127.2(3)	4.3(7)				

TABLE IV. *(Continued.)*

E_{level} (keV)	J^{π}	E_{γ} (keV)	I_{γ}	a_2	a_4	DCO	ΔJ
		1565.2(3)	0.8(3)				
4644.2(5)		512.8(1)	3.0(3)				
4780.8(4)	(12)	722.0(2)	10.7(5)				
		1734.2(6)	6.6(7)				
5001.1(5)		1954.0(4)	1.9(5)				
5074.9(8)		2693.3(8)	2.2(7)				
5234.0(3)		702.0(1)	0.87(22)				
5261.1(3)	(12)	648.9(1)	10.7(6)				
		1239.0(3)	4.5(6)	>0			(2)
5985.0(13)		1926.3(12)	4.0(6)				
6026.2(3)	(13)	765.1(1)	7.2(5)				
		1414.0(4)	2.3(6)				
6107.4(4)	(13)	1326.6(2)	1.4(4)				
		2050(3)	3.1(15)	>0*			(2)*
6234.4(4)		1453.6(2)	1.9(4)				
6823.5(5)	(14)	716.0(3)	1.2(3)				
		2045.8(13)	7.4(15)	>0*			(2)*
6862.9(3)	(14)	836.7(1)	4.2(4)				
		1601.9(5)	4.7(7)				
7757.6(4)	(15)	894.6(1)	3.2(4)				
		1731.3(6)	2.8(9)				
8982.2(9)	(16)	2119.2(8)	3.5(10)				
9235(3)	(16)	2411(3)	2.2(6)				

A and B. The spectrum contains peaks corresponding to the most intense transitions in Band B (those with energies of 537, 590, and 649 keV), along with lower-lying transitions in Band A (those with energies of 103, 130, 249, 565, 569, and 665 keV) giving weight to the placement of these transitions proposed in Fig. 12.

The sequence labeled A in Fig. 12 appears to be composed of stretched-$E2$ and $\Delta J = 1$ crossover transitions. Of the latter, the 249-, 598-, 665-, and 1012-keV transitions have measured angular distributions with small, negative a_2 coefficients. The 1167-, 1263-, and 1677-keV transitions were found to have a_2 and a_4 coefficients consistent with a stretched-$E2$ character. A three-point angular distribution for the 2046/2050-keV doublet also indicates a positive a_2 coefficient. Alignment parameters extracted from these stretched-$E2$ transitions were combined with the a_2 coefficients of the crossover transitions to estimate their mixing ratios; $\delta \sim 0$ was determined for all cases. Tentative spin assignments are suggested by the

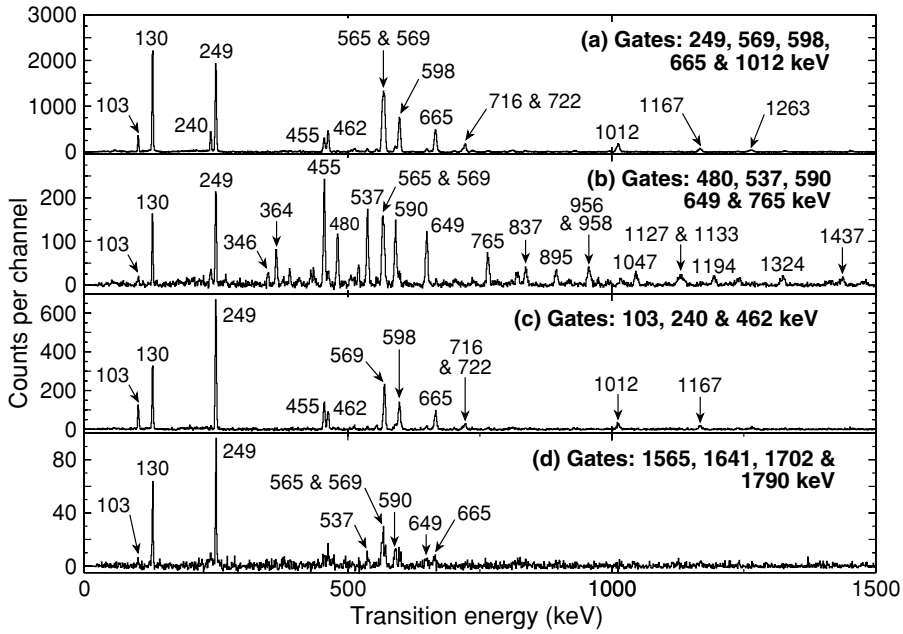

FIG. 13. ^{60}Mn-gated spectra obtained from recoil-$\gamma\gamma$ coincidences. Peaks are labeled by their energy to the nearest keV. The individual gated spectra have been summed together to generate the spectra shown here.

extension of this pattern to higher spin, when angular distributions were not possible.

As noted above, one of the $\Delta J = 1$ transitions in this structure, with an energy of 569 keV, forms an unresolved doublet with the 565-keV γ ray. Both the angular distribution and DCO ratio for the total intensity of the doublet indicate the possibility that $\Delta J = 1$ assignments are applicable to both transitions. In addition, a DCO ratio gated on the 1167-keV stretched-quadrupole transition, running parallel to the 569-keV γ ray, yields respective values of 0.7(3), 0.7(2), and 0.7(3) for the 130-, 249-, and 565-keV transitions, consistent with a $\Delta J = 1$ assignment for all.

In principle, the absolute spins of the levels in Band A can be determined by consideration of the transitions at the bottom of the band that feed the 4^+ isomer. However, each of these is somewhat ambiguous, allowing only tentative assignments. The dipolar nature of the 565-keV transition cannot be deduced in isolation from the 569-keV line, as noted above, but gives a tentative spin assignment of $5\hbar$ to the level at 836 keV. Using the assignments of the 103- and 130-keV transitions as dipoles, the states at 733 and 965 keV can be given tentative spin assignments of 4 and $6\hbar$, respectively. This would imply that the 462-keV transition deexciting the 733-keV state to the 4^+ isomer is $\Delta J = 0$; the measured positive a_2 coefficient is consistent with a folded-dipolar transition. For the 965-keV state, which decays via the level at 726 keV, it is also difficult to to make concrete assignments; the 240-keV transition from the state at 965 keV has an a_2 coefficient consistent with a dipole nature implying that the 455-keV transition following on to the isomer is $\Delta J = 1$. The a_2 coefficient for this transition is positive, indicating a moderately mixed transition.

Spin assignments in Band B are largely tentative, being based on the small number of angular distributions that were possible to measure, combined with restrictions placed on spins from parallel-decay pathways and yrast-feeding arguments.

4. ^{60}Mn *shell-model calculations*

There is insufficient experimental information on ^{60}Mn to assign parities beyond the known 1^+ and 4^+ lowest-lying states. However, some states at low excitation energy do appear to correspond, at least in energy, to levels predicted by shell-model calculations. These states are compared to the predictions of the GXPF1A Hamiltonian in Fig. 14. However, it is difficult to test thoroughly the accuracy of the shell-model calculations for the $A = 60$ isotope.

The unambiguous $J^\pi = 1^+$ and 4^+ assignments to the ground state and 271-keV level from Ref. [23] are reproduced well by the shell-model predictions; the latter lies within just 34 keV of its theoretical counterpart. The states at 726, 1090, and 2049 keV are proposed to correspond to the 5_1^+, 6_1^+, and 7_1^+ states, respectively, due to the reasonable agreement in the energies and γ-branching ratios between the experimental results and theoretical predictions. Note that the 965-keV level is *not* interpreted as the yrast 6^+ state, despite the fact that it lies only 1 keV above the closest $J = 6$ theoretical counterpart. This is due to the fact that the calculations predict a significant γ-ray branch to the 4_1^+ state that is not observed experimentally. The breakdown in agreement between theory and experiment for the states above 964 keV is much more clear. For example, the $J = 7$ state at 1215 keV lies over 750 keV below the predicted 7_1^+ state, and almost certainly contains admixtures of configurations involving orbitals outside the fp model space. The magnitude of the discrepancies increases further at higher spin. In addition, the respective $J = 4$ and 5 states at 733 and 836 keV have no reasonable shell-model analogs, and these states are assumed to be part of Sequence A as well.

The respective 3_1^+ and 2_1^+ calculated states at 53 and 100 keV have no obvious experimental counterparts and there appears to be somewhat of a breakdown in the predictive power of the GXPF1A Hamiltonian. The observed discrepancies may be due to an unreasonably large $\nu 2p_{1/2}$-$\nu 1f_{5/2}$ energy gap in the case of the $A = 60$ isotope. In fact, none of the calculated $2_1^+, 3_1^+, 3_2^+, 4_2^+$, or 5_2^+ states, which are all dominated by $\nu(1f_{5/2})^2(2p_{1/2})^1$ configurations, have clear experimental counterparts. Calculations imply that the energy gap between the $\nu 2p_{1/2}$ and $\nu 1f_{5/2}$ orbits must be reduced for the calculated 3_1^+ and 2_1^+ states to become reasonable counterparts of the experimental levels at 757 and 841 keV. Such modifications to the single-particle orbits are important in the case of ^{60}Mn, as the GXPF1A interaction does not successfully model the isomeric nature of the 4_1^+ state; the bare single-particle energy of the $\nu 1f_{5/2}$ orbital must be lowered by approximately 0.5 MeV to shift the $2, 3_1^+$ states above the yrast 4^+ state. Observations like these may highlight the changes that occur in single-particle orbitals away from the valley of stability.

In general, the shell-model calculations are not as successful for ^{60}Mn as for the lighter isotopes. Such a breakdown was observed in the cases of the heavier Cr and Fe nuclei

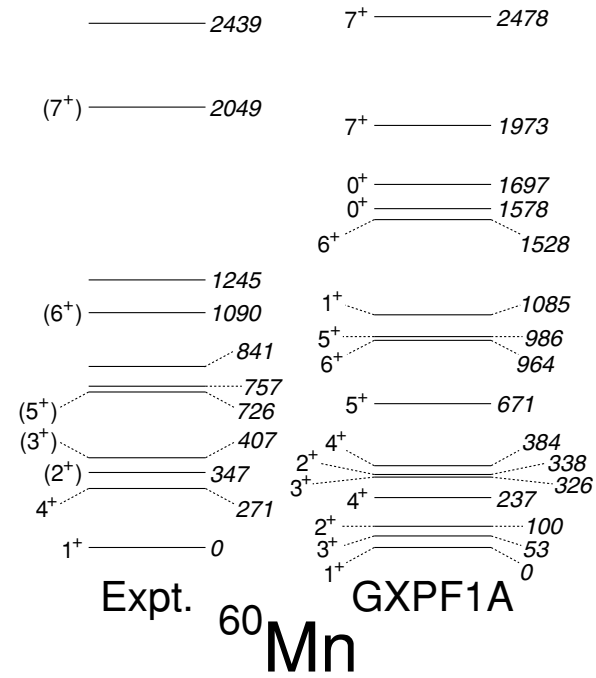

FIG. 14. GXPF1A shell-model calculations for ^{60}Mn compared with candidates for positive-parity states from the current work.

as well [13–15] and is, therefore, not too surprising. Such observations indicate that the adopted fp model space is simply too restrictive for proper use in the more exotic, neutron-rich isotopes. In particular, the two regular coupled structures, Bands A and B, which form the majority of the level scheme, find no counterparts within the fp model space. It is, therefore, likely that these structures involve excitations of $1g_{9/2}$ neutrons. Furthermore, it is interesting to speculate whether Bands A and B may involve one and two $\nu 1g_{9/2}$ excitations, given the fact that the former appears at relatively low excitation energy.

5. *Comparison of the* ^{58,60}Mn *level schemes*

It can be seen from Figs. 9 and 12 that the structures of the two even-A isotopes display, in the same fashion as ^{57,59}Mn, some similarity in their level schemes. In both cases, low-lying 4^+ isomeric states have been identified above a 1^+ ground state and coupled quasirotational structures of likely negative parity have been observed at higher spin. It is interesting to note that a similar high-spin structure is also present in ^{56}Mn [37]. Despite the fact that the spins and parities associated with the states in the ^{56,58,60}Mn quasirotational structures are tentative, it appears that the level sequence of interest, as a whole, simply shifts down in energy as the neutron number increases. It is, therefore, likely that the ^{56}Mn level at 2273 keV [37] is the analog of the 1601- and 965-keV spin-6 states in ^{58}Mn and ^{60}Mn, respectively, from the observed γ-ray energy and intensity systematics. Note that the 2273-keV state was tentatively assigned $J^\pi = 5^-$ or 6^- in Ref. [37], while those at higher energy were proposed values based solely on systematics. Such shifts appear consistent with the naive expectation that the Fermi surface approaches the $\nu 1g_{9/2}$ orbital with increasing N. These observations are similar to those in the neutron-rich Cr isotopes, where the energy of the first $9/2^+$ state in ^{55,57,59}Cr is observed to decrease from 2087 keV at $N = 31$ [38], through 1507 keV at $N = 33$ [14] to 503 keV at $N = 35$ [18].

Plots of aligned angular momentum as a function of rotational frequency for the bands built above the 1338- and 733-keV states in ^{58,60}Mn are shown in Fig. 15. Their close resemblance emphasizes the similarity between the sequences. The magnitude of the aligned angular momentum appears consistent with a configuration involving one $1g_{9/2}$ neutron. Furthermore, the fall in excitation energy from 1338 to 733 keV also appears to be consistent with such a structure. There is a notable lack of upbends or changes in alignment in both cases, which may be suggestive of a reasonable magnitude of deformation. Additional evidence might have arisen from consideration of band termination, but in these cases, the sequences are not populated to spins comparable to the exhaustion of spin in the suggested configurations, similar to the case of a proposed 2p-2h structure in ^{60}Fe [15].

Given this interpretation, it is interesting to speculate whether the appearance of an additional coupled band (Band B) in ^{60}Mn involves a similar configuration, or an additional $1g_{9/2}$ neutron excitation facilitated by the movement of the Fermi surface toward that orbital.

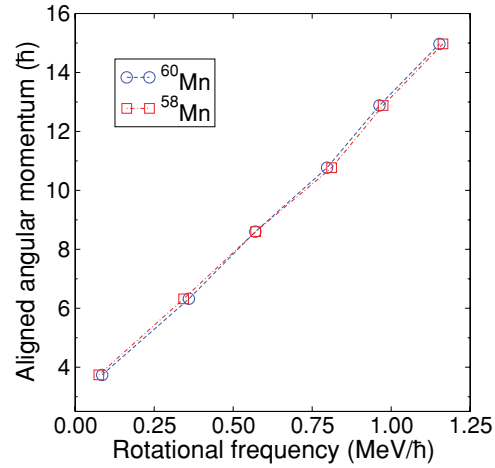

FIG. 15. (Color online) Aligned-angular-momenta plots for the proposed negative-parity bands built above the tentative $4\hbar$ states at 1338 and 733 keV in ^{58,60}Mn, respectively. $K = 4$ has been assumed in both cases.

It is also worth noting that the gradient of the lines in Fig. 15 falls between the values for Cr and Fe, suggesting that a systematic change in the magnitude of deformation occurs as protons are added to the $1f_{7/2}$ orbital.

IV. ONSET OF COLLECTIVITY: THE $\nu 1g_{9/2}$ ORBITAL

Previous studies of neutron-rich fp-shell nuclei provide strong evidence for the shape-driving potential of the $\nu 1g_{9/2}$ orbital. For example, quasirotational bands have been observed in neutron-rich $_{24}$Cr [13,14] and $_{26}$Fe [15] isotopes as a consequence of neutron excitations across the weak $N = 40$ subshell closure. As these two nuclear species neighbor the $_{25}$Mn isotopes, it is reasonable to expect similar structures from population of the $\nu 1g_{9/2}$ intruder orbital in the level schemes presented in this study.

Indeed, quasicollective bands present themselves in the structures of $^{57-60}$Mn in a robust way. Importantly, the states associated with these structures cannot be easily interpreted in terms of shell-model calculations performed using the GXPF1A effective interaction, indicating that nucleon excitations beyond the adopted fp model space are likely to have taken place. Many of the states not reproduced well by the theoretical predictions are, therefore, assumed to be of unnatural parity for the fp model space; it is proposed here that the states that form the rotational-like structures result from neutron excitations involving the deformation-driving $\nu 1g_{9/2}$ orbital. However, it must be stressed that further work is required on the experimental front to confirm the parities of these states. One possibility resides in measurements of polarization coefficients for the γ-ray transitions. In addition, on the theoretical side, inclusion of the $\nu 1g_{9/2}$ intruder state in the shell-model calculations may prove to be especially useful for helping to identify states of unnatural parity. Although the GXPF1A Hamiltonian is currently under development to include the full $fpg_{9/2}$ model space, it is generally not capable of reproducing experimental results with great accuracy at the

present time. The preliminary results do, however, indicate a promising compression of the natural-parity states relative to the calculations that are restricted to the fp shell alone, particularly in the more exotic systems.

V. SUMMARY

The neutron-rich isotopes $^{57-60}$Mn have been studied using two separate heavy-ion fusion-evaporation reactions with 130-MeV ^{48}Ca beams on isotopically enriched ^{13,14}C targets.

The experimental results were compared to the predictions of large-scale shell-model calculations to test the accuracy of the GXPF1A effective interaction in a full fp model space. The shell-model Hamiltonian generally accounts for the negative-parity states in ^{57}Mn in a satisfactory manner; however, the level of agreement tends to decrease somewhat by the $N = 35$ isotope. In all cases, it is found that the addition of at least the $1g_{9/2}$ intruder state to the fp model space is desirable to reproduce the experimental systematics more accurately.

In common with other nuclei in this region, the occurrence of regular, rotational-like structures, which fall in excitation energy with increasing neutron number, is associated with excitations involving the $\nu 1g_{9/2}$ orbital. There is a clear need for both collective- and shell-model calculations that include this orbit to be developed in this neutron-rich region if a better understanding of the nuclear structure is to emerge.

ACKNOWLEDGMENTS

This work was supported by the UK Science and Technology Facilities Council (STFC), the US Department of Energy, Office of Nuclear Physics, under Contract Nos. DE-AC02-06CH11357 and DE-FG02-94ER40848, and the US National Science Foundation under Grant PHY-0139950. D. Steppenbeck and A. N. Deacon acknowledge financial support from RIKEN and STFC, respectively. The authors also thank M. Freer at the University of Birmingham for the use of the ^{14}C target.

[1] A. Huck, G. Klotz, A. Knipper, C. Miehé, C. Richard-Serre, G. Walter, A. Poves, H. L. Ravn, and G. Marguier, Phys. Rev. C **31**, 2226 (1985).
[2] A. Gade, R. V. F. Janssens, D. Bazin, R. Broda, B. A. Brown, C. M. Campbell, M. P. Carpenter, J. M. Cook, A. N. Deacon, D.-C. Dinca *et al.*, Phys. Rev. C **74**, 021302(R) (2006).
[3] R. V. F. Janssens, B. Fornal, P. F. Mantica, B. A. Brown, R. Broda, P. Bhattacharyya, M. P. Carpenter, M. Cinausero, P. J. Daly, A. D. Davies *et al.*, Phys. Lett. **B546**, 55 (2002).
[4] J. J. Prisciandaro, P. F. Mantica, B. A. Brown, D. W. Anthony, M. W. Cooper, A. Garcia, D. E. Groh, A. Kornives, W. Kumarasiri, P. A. Lofy *et al.*, Phys. Lett. **B510**, 17 (2001).
[5] D.-C. Dinca, R. V. F. Janssens, A. Gade, D. Bazin, R. Broda, B. A. Brown, C. M. Campbell, M. P. Carpenter, P. Chowdhury, J. M. Cook *et al.*, Phys. Rev. C **71**, 041302(R) (2005).
[6] A. Bürger, T. R. Saito, H. Grawe, H. Hübel, P. Reiter, J. Gerl, M. Górska, H. J. Wollersheim, A. Al Khatib, A. Banu *et al.*, Phys. Lett. **B622**, 29 (2005).
[7] T. Otsuka, T. Suzuki, R. Fujimoto, H. Grawe, and Y. Akaishi, Phys. Rev. Lett. **95**, 232502 (2005).
[8] M. Honma, T. Otsuka, B. A. Brown, and T. Mizusaki, Phys. Rev. C **65**, 061301(R) (2002).
[9] B. Fornal, S. Zhu, R. V. F. Janssens, M. Honma, R. Broda, P. F. Mantica, B. A. Brown, M. P. Carpenter, P. J. Daly, S. J. Freeman *et al.*, Phys. Rev. C **70**, 064304 (2004).
[10] M. Honma, T. Otsuka, B. A. Brown, and T. Mizusaki, Eur. Phys. J. A **25**, 499 (2005).
[11] S. Zhu, R. V. F. Janssens, B. Fornal, S. J. Freeman, M. Honma, R. Broda, M. P. Carpenter, A. N. Deacon, B. P. Kay, F. G. Kondev *et al.*, Phys. Lett. **B650**, 135 (2007).
[12] A. N. Deacon, D. Steppenbeck, S. Zhu, S. J. Freeman, R. V. F. Janssens, M. P. Carpenter, B. Fornal, M. Honma, B. P. Kay, F. G. Kondev, J. Kozemczak, A. Larabee, T. Lauritsen, C. J. Lister, A. P. Robinson, D. Seweryniak, J. F. Smith, X. Wang, and F. R. Xu (in preparation).
[13] S. Zhu, A. N. Deacon, S. J. Freeman, R. V. F. Janssens, B. Fornal, M. Honma, F. R. Xu, R. Broda, I. R. Calderin, M. P. Carpenter *et al.*, Phys. Rev. C **74**, 064315 (2006).
[14] A. N. Deacon, S. J. Freeman, R. V. F. Janssens, F. R. Xu, M. P. Carpenter, I. R. Calderin, P. Chowdhury, N. J. Hammond, T. Lauritsen, C. J. Lister *et al.*, Phys. Lett. **B622**, 151 (2005).
[15] A. N. Deacon, S. J. Freeman, R. V. F. Janssens, M. Honma, M. P. Carpenter, P. Chowdhury, T. Lauritsen, C. J. Lister, D. Seweryniak, J. F. Smith *et al.*, Phys. Rev. C **76**, 054303 (2007).
[16] J. J. Valiente-Dobón, S. M. Lenzi, S. J. Freeman, S. Lunardi, J. F. Smith, A. Gottardo, F. Della Vedova, E. Farnia, A. Gadea, D. R. Napoli *et al.*, Phys. Rev. C **78**, 024302 (2008).
[17] D. E. Appelbe, R. A. E. Austin, G. C. Ball, J. A. Cameron, B. Djerroud, T. E. Drake, S. Flibotte, C. D. O'Leary, A. Melarangi, C. E. Svensson *et al.*, Eur. Phys. J. A **8**, 153 (2000).
[18] S. J. Freeman, R. V. F. Janssens, B. A. Brown, M. P. Carpenter, S. M. Fischer, N. J. Hammond, M. Honma, T. Lauritsen, C. J. Lister, T. L. Khoo *et al.*, Phys. Rev. C **69**, 064301 (2004).
[19] I. Y. Lee, Nucl. Phys. **A520**, 641c (1990).
[20] C. N. Davids, B. B. Back, K. Bindra, D. J. Henderson, W. Kutschera, T. Lauritsen, Y. Nagame, P. Sugathan, A. V. Ramayya, and W. B. Walters, Nucl. Instrum. Methods B **70**, 358 (1992).
[21] S. N. Liddick, P. F. Mantica, R. Broda, B. A. Brown, M. P. Carpenter, A. D. Davies, B. Fornal, M. Horoi, R. V. F. Janssens, A. C. Morton *et al.*, Phys. Rev. C **72**, 054321 (2005).
[22] E. Runte, K.-L. Gippert, W.-D. Schmidt-Ott, P. Tidemand-Petersson, and L. Ziegeler, Nucl. Phys. **A441**, 237 (1985).
[23] S. N. Liddick, P. F. Mantica, B. A. Brown, M. P. Carpenter, A. D. Davies, M. Horoi, R. V. F. Janssens, A. C. Morton, W. F. Mueller, J. Pavan *et al.*, Phys. Rev. C **73**, 044322 (2006).
[24] T. E. Ward, P. H. Pile, and P. K. Kuroda, Nucl. Phys. **A134**, 60 (1969).
[25] K. G. Tirsell, L. G. Multhauf, and S. Raman, Phys. Rev. C **10**, 785 (1974).
[26] J. F. Mateja, C. P. Browne, C. E. Moss, and J. B. McGrory, Phys. Rev. C **15**, 1708 (1977).
[27] C. N. Davids, D. F. Geesaman, S. L. Tabor, M. J. Murphy, E. B. Norman, and R. C. Pardo, Phys. Rev. C **17**, 1815 (1978).

[28] J. F. Majeta, G. F. Neal, J. Goss, P. R. Chagnon, and C. P. Browne, Phys. Rev. C **13**, 118 (1976).
[29] K. A. Aniol, D. W. Gebbie, C. L. Hollas, and J. Nurzynski, Nucl. Phys. **A303**, 154 (1978).
[30] M. Oinonen, U. Köster, J. Äystö, V. Fedoseyev, V. Mishin, J. Huikari, A. Jokinen, A. Nieminen, K. Peräjärvi, A. Knipper *et al.*, Eur. Phys. J. A **10**, 123 (2001).
[31] T. E. Ward, P. H. Pile, and Kuroda, Phys. Rev. **182**, 1186 (1969).
[32] N. C. Dyer and J. H. Hamilton, Nucl. Phys. **A173**, 393 (1971).
[33] U. Bosch, W.-D. Schmidt-Ott, E. Runte, P. Tidemand-Petersson, P. Koschel, F. Meissner, R. Kirchner, O. Klepper, E. Roeckl, K. Rykaczewski *et al.*, Nucl. Phys. **A477**, 89 (1988).
[34] W. D. Schmidt-Ott, K. Becker, U. Bosch-Wicke, T. Hild, F. Meissner, R. Kirchner, E. Roeckl, and K. Rykaczewski, in *Proceedings 6th Intern. Conf. on Nuclei Far from Stability + 9th Intern. Conf. on Atomic Masses and Fundamental Constants, Bernkastel-Kues, Germany* (1993), edited by R. Neugart and A. Wohr (Institute of Physics, Bristol, 1993), p. 627.
[35] M. R. Bhat, Nucl. Data Sheets **80**, 789 (1997).
[36] E. B. Norman, C. N. Davids, M. J. Murphy, and R. C. Pardo, Phys. Rev. C **17**, 2176 (1978).
[37] A. M. Nathan, J. W. Olness, E. K. Warburton, and J. B. McGrory, Phys. Rev. C **16**, 192 (1977).
[38] D. E. Appelbe, C. J. Barton, M. H. Muikku, J. Simpson, D. D. Warner, C. W. Beausang, M. A. Caprio, J. R. Cooper, J. R. Novak, N. V. Zamfir *et al.*, Phys. Rev. C **67**, 034309 (2003).